Publication Year	2023
Acceptance in OA	2024-10-31T10:39:19Z
Title	The Hateful Eight: Connecting Massive Substructures in Galaxy Clusters like A2744 to Their Dynamical Assembly State Using the Magneticum Simulations
Authors	Kimmig, Lucas C., Remus, Rhea Silvia, Dolag, Klaus, BIFFI, Veronica
Publisher's version (DOI)	10.3847/1538-4357/acc740
Handle	http://hdl.handle.net/20.500.12386/35357
Journal	THE ASTROPHYSICAL JOURNAL
Volume	949

The Astrophysical Journal, 949:92 (21pp), 2023 June 1 https://doi.org/10.3847/1538-4357/acc740

The Hateful Eight: Connecting Massive Substructures in Galaxy Clusters like A2744 to Their Dynamical Assembly State Using the Magneticum Simulations

Lucas C. Kimmig[1], Rhea-Silvia Remus[1], Klaus Dolag[1,2], and Veronica Biffi[1,3]

[1] Universitäts-Sternwarte München, Fakultät für Physik, LMU München, Scheinerstr. 1, D-81679 München, Germany; lkimmig@usm.lmu.de
[2] Max-Planck-Institute for Astrophysics, Karl-Schwarzschild-Str. 1, D-85748 Garching, Germany
[3] INAF—Osservatorio Astronomico di Trieste, via Tiepolo 11, I-34143 Trieste, Italy

Received 2022 September 20; revised 2023 March 10; accepted 2023 March 22; published 2023 June 1

Abstract

Substructures are known to be good tracers for the dynamical states and recent accretion histories of the most massive collapsed structures in the universe, galaxy clusters. Observations find extremely massive substructures in some clusters, especially Abell 2744 (A2744), which are potentially in tension with the ΛCDM paradigm because they are not found in simulations directly. However, the methods to measure substructure masses strongly differ between observations and simulations. Using the fully hydrodynamical cosmological simulation suite MAGNETICUM PATHFINDER, we develop a method to measure substructure masses in projection from simulations, similarly to the observational approach. We identify a simulated A2744 counterpart that not only has eight substructures of similar mass fractions but also exhibits similar features in the hot gas component. This cluster formed only recently through a major merger together with at least six massive minor merger events since $z = 1$, where previously the most massive component had a mass of less than $1 \times 10^{14} M_\odot$. We show that the mass fraction of all substructures and of the eighth substructure separately are excellent tracers for the dynamical state and assembly history for all galaxy cluster mass ranges, with high fractions indicating merger events within the last 2 Gyr. Finally, we demonstrate that the differences between subhalo masses measured directly from simulations as bound and those measured in projection are due to methodology, with the latter generally 2–3 times larger than the former. We provide a predictor function to estimate projected substructure masses from SUBFIND masses for future comparison studies between simulations and observations.

Unified Astronomy Thesaurus concepts: Galaxy clusters (584); Galaxy formation (595); Computational methods (1965); Cold dark matter (265)

1. Introduction

Galaxy clusters come in many different flavors: from relaxed clusters with smooth hot X-ray halos and a clearly identifiable brightest cluster galaxy (BCG), like A383 (e.g., Allen et al. 2008), to highly disturbed systems with detectable shock fronts and multiple massive galaxies, like Abell 2744 (A2744) (e.g., Jauzac et al. 2016) or MACS J0416.1-2403 (e.g., Grillo et al. 2015). Their dynamical states are commonly linked to their recent accretion history—and are thought to reflect the state of their cosmic environment, given that they mark the nodes of the collapsing cosmic web.

Galaxy cluster substructures are some of the best indicators to provide insights into both the dynamical state (e.g., De Lucia et al. 2004; Neto et al. 2007; Biffi et al. 2016) and the accretion history (e.g., Jiang & van den Bosch 2016) of their host galaxy clusters, as well as providing a test for potential dark matter variants (Bhattacharyya et al. 2021) and cosmological parameters (e.g., Ragagnin et al. 2021). Recent gravitational lensing observations of galaxy cluster substructures have posed challenges to the ΛCDM paradigm, due to discrepancies found between the observations and cosmological simulations: The observed substructure masses are found to be larger (e.g., Jauzac et al. 2016; Schwinn et al. 2017), especially in the central regions (Grillo et al. 2015), and they appear to be more concentrated (e.g., Meneghetti et al. 2020; Ragagnin et al. 2022). While the differing concentration is not resolved purely from the inclusion of baryonic physics (Munari et al. 2016), it has been postulated that it may arise from the exact included baryonic subgrid physics in simulations (Bahé 2021). The higher observed masses, in turn, are thought to possibly arise from projection effects, albeit this has so far only been tested using dark matter only simulations (Mao et al. 2018; Schwinn et al. 2018). Therefore, to enable future joint investigations employing both hydrodynamical simulations and gravitational lensing observations, it is necessary to understand the relationship between the intrinsic, three-dimensional substructure identification from simulations and the projected substructure masses, which we will analyze in this study.

An excellent testing ground for this endeavor is provided by the particularly extreme case of galaxy cluster A2744 at $z = 0.308$, with eight substructure masses measured by Jauzac et al. (2016) to all contain masses in excess of $5 \times 10^{13} M_\odot$ within 150 kpc apertures. In addition, the substructures are all located in close proximity within a sphere with a radius of 1 Mpc. This cluster has also been mapped in X-ray and radio bands, detecting both strong shock fronts (e.g., Owers et al. 2011; Eckert et al. 2015) in combination with radio relics (e.g., Giovannini et al. 1999; Eckert et al. 2016; Rajpurohit et al. 2021). All these detection have been interpreted as the results of at least one massive recent merger event (e.g., Kempner & David 2004; Boschin et al. 2006), if not even multiple merger events (e.g., Merten et al. 2011). As part of the Hubble Frontier Field program (Lotz et al. 2017), A2744 is one of the best-studied and most deeply imaged galaxy clusters, with multiple studies on its strong and weak lensing properties (e.g., Jauzac et al. 2016; Bird & Goldberg 2018; Mahler et al. 2018). In addition, A2744 is part of the GLASS-JWST program (Treu et al. 2022), and as such, more detailed studies on its properties are to be expected soon, especially with regard to strong lensing (Bergamini et al. 2022).

In this study, we aim to identify an A2744 counterpart in a fully hydrodynamical cosmological simulation, with all baryonic physics included. This will conclusively answer the question of whether the large substructure masses observed by strong lensing measurements are really in tension with the ΛCDM paradigm, or if this tension can be solved when accounting for projection effects. We further analyze whether projected substructure masses can still be used as a tracer for the accretion history of the host galaxy cluster.

To this end, we utilize the fully hydrodynamical cosmological simulation suite Magneticum Pathfinder, which is presented in Section 2. In Section 3, we introduce a method to identify substructures in projections similar to what is possible observationally, and we compare the resulting substructure masses to those obtained as bound subhalos directly from the simulation output in Section 4. The method will be used to identify A2744 counterparts in the simulation in Section 5. We analyze its formation pathways in Section 5.1, and generalize the results over all galaxy cluster mass ranges above $M_{\rm vir} \geqslant 1 \times 10^{14} M_\odot$ in Section 5.2, connecting the projected substructure mass fractions to the dynamical state of galaxy clusters (Section 5.3). Finally, we summarize and conclude this study in Section 6.

2. Simulation

The employed simulation is the fully hydrodynamical cosmological simulation Magneticum Pathfinder[4] (K. Dolag et al. 2023, in preparation), following a WMAP-7 cosmology as $\Omega_0 = 0.272$ and $h = 0.704$ from Komatsu et al. (2011). All simulations were performed using an updated version of the Tree-PM SPH-code GADGET-2 (Springel 2005), with SPH modifications according to Dolag et al. (2004, 2005), Donnert et al. (2013), and Beck et al. (2016). Employed physics include star formation, metal enrichment, and cooling processes (Tornatore et al. 2004, 2007; Wiersma et al. 2009), as well as AGN feedback (Fabjan et al. 2010; Hirschmann et al. 2014). The details are discussed in more depth by Teklu et al. (2015) and Dolag et al. (2017). Magneticum Pathfinder reproduces global galaxy properties well, such as angular momentum (Teklu et al. 2015; Schulze et al. 2018) and density distributions (Remus et al. 2017; Harris et al. 2020; Remus & Forbes 2022), properties of galaxies in cluster environments (Lotz et al. 2019, 2021), as well as X-ray emission from galaxy clusters (Biffi et al. 2018).

The boxes cover a wide range of resolutions and sizes. As in this study, the substructures of the most massive galaxy clusters are investigated, Box2b/hr is chosen because, with a box volume of (909 cMpc)^3, it is sufficiently large to contain galaxy clusters in excess of $M_{\rm FOF} > 1 \times 10^{15} M_\odot$ at a redshift comparable to that of A2744. Simultaneously, with a mean stellar particle resolution of $4.97 \times 10^7 M_\odot$, it resolves halos with at least 100 stellar particles down to a total stellar mass of $M_* \geqslant 5 \times 10^9 M_\odot$. These galaxy clusters from the Magneticum Pathfinder simulation suite can also be accessed through the web portal;[5] see Ragagnin et al. (2017) for more details.

Table 1
Summary of the Mass Bins Used

Mass Bin	Mass Range ($10^{14} M_\odot$)	$\bar{M}_{\rm vir}$ ($10^{14} M_\odot$)
Giants	$M_{\rm FOF} > 10$	13.13
Medium	$5.15 > M_{\rm vir} > 4.85$	5.002
Small	$2.01 > M_{\rm vir} > 1.99$	2.000
Tiny	$1.002 > M_{\rm vir} > 0.998$	1.000

Notes. Each contains the first 29 galaxy clusters within the specified mass range, as sorted by their friend-of-friends mass.

At a redshift of $z \approx 0.252$, to be compatible with that of A2744, halos were identified using the baryonic version of the halofinder SUBFIND (Dolag et al. 2009), which uses a binding criterion to select particles belonging to the halos. To ensure a broad mass range of galaxy clusters considered, four mass bins of 29 galaxy clusters each are selected. The first, henceforth "giants," comprises the most massive 29 galaxy clusters as defined by their friends-of-friends mass, where all have $M_{\rm FOF} > 1 \times 10^{15} M_\odot$. Then the bins "medium," "small," and "tiny" are chosen such that their respective mean virial masses are tightly distributed around 5, 2, and $1 \times 10^{14} M_\odot$. The mass bins are summarized in Table 1.

3. Method: Cylinder Projection

The goal is to develop a method similar to the procedures from gravitational lensing observations, while remaining within the raw particle data and minimizing model assumptions. For such lensing analyses, one typically differentiates between a cluster-scale overdensity and many smaller galaxy-scale overdensities. These are commonly modeled by dPIE density profiles, as introduced by Kassiola & Kovner (1993). However, implementation of lenses via models within the simulations would require a large amount of additional assumptions. Instead, we assume that the lensing models can, as postulated, capture the real underlying mass distribution successfully, and therefore we focus on the aspect of bound versus projected mass distributions. From the simulation side, it is possible to separate stellar and dark matter particles that form an individual bound (sub)structure from those particles that are only bound to the full structure potential; however, this is impossible in observations. Additionally, observations by their nature can only provide projected information, representing one of the largest differences versus simulations. Thus, we will in the following introduce the method used here to analyze the simulation as closely to the observational procedure as possible without implementing model assumptions, and compare it to the information obtained directly from the simulation.

3.1. Mass Maps

The starting point for obtaining the projected substructure masses is a projected mass map. Mass particles from the simulation are projected onto a plane with a depth of $r_z \approx 5 \cdot r_{\rm vir}$ in front and behind the galaxy cluster. Even for the largest galaxy clusters of the "giants," this is more shallow than typical spectroscopic criteria employed in gravitational lensing analyses (e.g., Jauzac et al. (2016), where the spectroscopic depth criterion equates to around $r_z \approx 38$ Mpc $\approx 15 \cdot r_{\rm vir}$). It should be noted that we find the exact projection depth beyond $1 \cdot r_{\rm vir}$ to have negligible impact on the results; see Appendix B.

---

[4] www.magneticum.org

[5] https://c2papcosmosim.uc.lrz.de

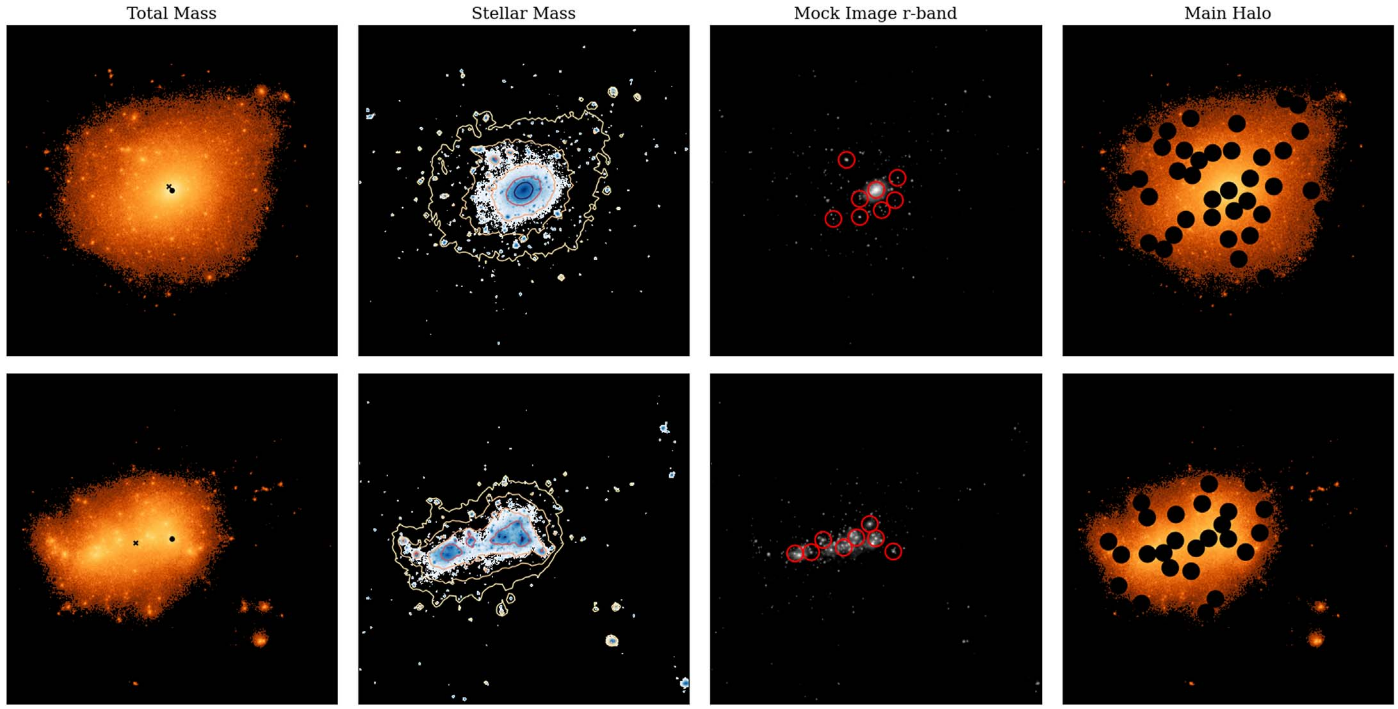

Figure 1. Examples of surface mass density and brightness maps for "giant" galaxy clusters 5 (top) and 20 (bottom) at a redshift of $z = 0.252$. Left: projected total mass map, with the SUBFIND cluster center (i.e., the most-bound-particle position) indicated as a black dot and the projected center of mass marked with a cross. The colorbar range is $-3.7 < \log_{10}(\Sigma[10^{10}M_{\odot}]) < 0.1$. Center left: the stellar mass map, with isodensity lines of the total mass map. The colorbar range is $-6 < \log_{10}(\Sigma[10^{10}M_{\odot}]) < -1$. Center right: mock image in the r band as seen from $z = 0$ down to a limiting magnitude of 25 mag, generated via the method from Martin et al. (2022). The red circles denote the eight most massive identified substructures. Right: total mass map with identified substructures masked out, leaving the main halo.

The projection angle is arbitrary, but the resulting quantities could vary strongly with projection. Thus, for each galaxy cluster, 200 projections are sampled from an isotropical distribution on a spherical surface, resulting in 5800 projections of galaxy clusters in total per cluster mass bin. The initial projected map is centered on the most bound particle as determined by SUBFIND, which is a common choice of center for structure finders, as this coincides with the deepest point of the potential well of the cluster.

This position must *not* equal the center of mass, though it can be the same for a smooth, undisturbed, continuous mass distribution. Instead, the center of mass is determined from the projected total particle data directly via a shrinking sphere algorithm based on the work by Power et al. (2003). The resulting barycenters are largely independent of initial parameters, so long as a sufficiently large initial area is used. Here, the initial area is chosen as a circle of radius $1 \cdot r_{\mathrm{vir}}$, and the barycenter is determined then in 2D. The shrinking factor is $f_{\mathrm{shrink}} = 0.975$, as given by Power et al. (2003). A lower limit of 1000 particles within the circle is used as a break-off criterion for the algorithm. Alternatively, the algorithm ends if between iterations the barycenter varies less than two times the softening length of the dark matter.

To highlight the differences, the first column of Figure 1 illustrates both the SUBFIND galaxy cluster center (black circle) and the projected center of mass (black cross) for two example galaxy clusters from the "giants" mass bin, cluster 5 (top row) and cluster 20 (bottom row). Shown is an area of $(6\,\mathrm{Mpc})^2$. For the first cluster, the projected center of mass is similar to the center from SUBFIND, while there exists a stark difference for the second cluster, which is much more elongated and in a state of assembly. Here, the deviation reaches on the order of half the virial radius. Therefore, this clearly highlights the importance of finding the center of mass when comparing to observations.

3.2. Identifying Substructure

Considering the substructure within the galaxy clusters, first a distinction must be made. The gravitationally bound structures as identified by SUBFIND are referred to in the following as *subhalos* (with masses written as M_{sub}). This can mean both an individual galaxy but also a group of galaxies, if their gravitational attraction to each other is stronger than that to the host galaxy cluster. The group's combined potential is of course then still bound to the host. On the other hand, the projected masses within a given aperture are referred to as *substructures* (with masses written as M_{cyl}). A substructure may only appear close together, while being actually comprised of several separate objects. For the "giants," a single substructure can consist of 1–19 subhalos above a stellar mass of $4 \times 10^{10} M_{\odot}$. Most, however, contain just one or two galaxies. This is consistent with the observational approach to include in a substructure all galaxies within the aperture that belong to the cluster.

Potential positions of substructure are identified via the centers of subhalos from SUBFIND. To this end, all subhalos above a stellar mass cut $M_{*,\mathrm{cut}}$ are considered as initial positions. However, the subhalos may be elongated, and as such in projection could appear to have a shifted center relative to their most bound particles. Similarly, two subhalos overlapping in projection may appear as a single structure with a center between them. As galaxy-scale models within gravitational lensing analyses are placed based on the observed maps,

Table 2
Overview of the Relevant Parameters for Each Mass Bin Used

	Giants	Medium	Small	Tiny
$f_{\mathrm{m,scale}}$	1	0.381	0.152	0.076
r_{tot} [Mpc]	1.3	0.942	0.694	0.551
r_{ap} [kpc]	150.0	109	80.1	63.6
r_{conv}[kpc]	25.0	18.1	13.4	10.6
r_{pix} [kpc]	2.0	1.45	1.07	0.848
$M_{*,\mathrm{cut}}$ [$10^{10}M_{\odot}$]	4.0	1.524	0.609	0.5

Notes. Each mass bin is scaled relative to the "giants," according to their relative mean virial mass. The stellar mass cut used throughout is $M_{*,\mathrm{cut}}$, as indicated on the left in Figure 2, and the projection depth is $r_z \approx 5 \cdot r_{\mathrm{vir}}$.

i.e., based on the stellar mass, this process is mimicked via use of a projected stellar mass map. The centers of substructures are then determined by converging to the most massive stellar pixel within a given radius r_{conv} around the subhalo centers. This ensures that at least one real bound structure is within the aperture, while simultaneously accounting for how the structures appear in projection.

These potential substructure candidates are then sorted by their summed stellar masses within an area of $(9 \cdot r_{\mathrm{pix}})^2 = (18\ \mathrm{kpc})^2$ (scaled down for each bin as given in Table 2), and apertures are placed beginning with the most massive candidates. As apertures representing separate substructures should not overlap too strongly, this sorting ensures that the most massive obvious substructures are placed first. With an aperture radius of r_{ap}, the choice of minimum distance to already placed apertures of $d_{\min} = \sqrt{3} \cdot r_{\mathrm{ap}}$ ensures that at no point can three apertures overlap simultaneously.

Generally, the choice of aperture size r_{ap} is arbitrary, as one would need to know the mass of a substructure to obtain a representative radius for a structure of a given mass, while a radius is needed in order to measure the mass within to obtain a mass. Therefore, any given aperture could technically be chosen as a starting point. As one of the motivations to undertake this study is to test if we can reproduce the substructure properties of the galaxy cluster A2744, we chose the same aperture size for the "giants" clusters as that used by Jauzac et al. (2016), namely $r_{\mathrm{ap}} = 150$kpc. As this would be unphysically large for the smaller clusters, we scale the size of the aperture accordingly to the mass ratio of the virial masses of the "giants" to the smaller bin, i.e.,

$$r_{\mathrm{ap}} = 150\ \mathrm{kpc} \cdot \sqrt[3]{\bar{M}_{\mathrm{vir,i}}/\bar{M}_{\mathrm{vir,giants}}} = 150\ \mathrm{kpc} \cdot \sqrt[3]{f_{\mathrm{m,scale}}}\,. \quad (1)$$

The resulting values used for the different mass bins studied in this work can be found in Tables 1 and 2.

The stellar mass cut for potential candidates for substructures, $M_{*,\mathrm{cut}}$, is scaled linearly with the mean virial mass of the galaxy clusters, with a lower bound requiring that all substructures have sufficient particles, given the simulation resolution limits. Figure 2 shows the cumulative subhalo abundance for each of the four cluster mass bins, with the black solid line marking the stellar mass cut. Only for the smallest mass bin, the "tiny" clusters, does this threshold need to be shifted slightly to preserve the limit of at least 100 particles per subhalo, marked by the dashed–dotted black line. While on the one hand it can be seen that the subhalo number distributions of the clusters are generally self-similar, it can also be seen that the more massive galaxy clusters have significantly more subhalos with this threshold scheme, in agreement with actual observed galaxy clusters. For comparison, the horizontal dotted line marks a constant 25 subhalos, with the resulting mass ratio for each cluster mass bin marked by the vertical lines in the respective colors of the cluster mass bins.

Both middle columns of Figure 1 demonstrate the process of finding substructures, again for clusters 5 (top row) and 20 (bottom row) of the "giants." The second column shows the total stellar mass map, which in structure is very similar to the total mass maps shown on the left. Substructures are first identified as the centers of the subhalos above the stellar mass cut $M_{*,\mathrm{cut}}$ as per Table 2, and then shifted to the most massive pixels within the projected stellar mass map in the vicinity. The third column then depicts the resulting eight most massive substructures via red circles in a mock image representing what could be observed in the r band with a magnitude down to 26 mag using the method from Martin et al. (2022). All eight substructures include the brightest galaxies of both clusters visible in the r band. However, there are significantly more substructures identified overall. This can be seen in the right panel of Figure 1, where all substructures are marked by the black filled circles.

3.3. The Main Halo

Finally, the contribution to the total mass from the main halo needs to be determined for every projection. This is done by first masking the substructures, as demonstrated in the right column of Figure 1. Subsequently, the remaining particles are binned in 2D equal-mass bins, and the density within concentric rings is calculated. The resulting profile represents the main halo in projection and is found to be best fit by an Einasto profile (Einasto 1965), which is fit in the form:

$$\rho(r) = \rho_{-2} \exp\left\{-\frac{2}{\alpha_{\mathrm{Ein}}}\left[\left(\frac{r}{r_{-2}}\right)^{\alpha_{\mathrm{Ein}}} - 1\right]\right\}, \quad (2)$$

as given by Retana-Montenegro et al. (2012). The added flexibility from the slope parameter α_{Ein} allows better reproduction of the broad range of density profiles than the NFW profile (Navarro et al. 1996), even compared to fitting the projected NFW as given by Takada & Jain (2003).

Finally, the contribution from the mean cosmic background density ρ_{mean}, which is given by the sum of all mass divided by the box volume, must be subtracted as well. Consequently, the remaining mass within the apertures can be attributed solely to the substructures. The mass of substructures is then given by

$$\begin{aligned} M_{\mathrm{cyl,i}} &\equiv M_{\mathrm{ap,i}}^{\mathrm{substructure}} \\ &= M_{\mathrm{ap,i}} - [\rho_{\mathrm{Ein,fit}}(d_{\mathrm{i}}) + \rho_{\mathrm{mean}}] \cdot \pi r_{\mathrm{ap}}^2 \cdot r_{\mathrm{z}}, \end{aligned} \quad (3)$$

where $M_{\mathrm{ap,i}}$ is the summed mass of all particles within aperture i, $\rho_{\mathrm{Ein,fit}}(d_{\mathrm{i}})$ is the main halo density at the center of the aperture, and $\pi r_{\mathrm{ap}}^2 \cdot r_{\mathrm{z}}$ is the volume of the projected cylinder.

4. Bound versus Projected Masses

As mentioned, one of the major obstacles when comparing simulations with observations is the different dimensionality of the studied objects. Using the method outlined in Section 3, we can directly compare the values determined from the projection method with those resulting from bound structure via SUBFIND, thereby providing an estimate on how accurately the real

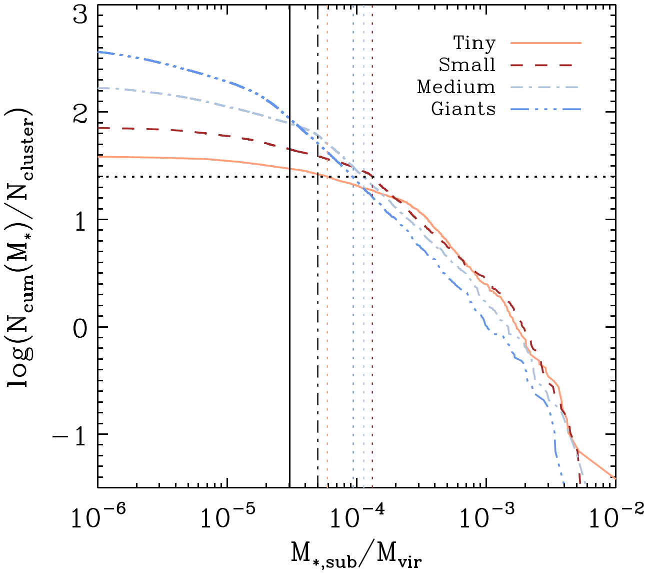

Figure 2. The logarithm with base 10 of the cumulative subhalo abundance per main halo in dependence on the subhalo stellar mass fraction of the main halo. Different colored lines represent the four mass bins. Vertical lines denote two different scalings of $M_{*,\mathrm{cut}}$. The solid black line scales linearly with the mean virial mass of the galaxy clusters, except for the "tinies" (black dashed–dotted) as they reach the resolution level of at least 100 stellar particles. The colored vertical lines instead scale such as to ensure an approximately constant number of apertures (≈25, indicated by the horizontal line).

underlying bound structures can be reconstructed from the 2D information.

4.1. Total Mass in Projection versus Bound Mass

The total mass fraction contained in substructures, i.e., in projected cylinder apertures, within a given radius relative to the total mass of the galaxy clusters is given as

$$f_{\mathrm{cyl}}(r) \equiv \left(\sum_{\mathrm{i}=2}^{N} M_{\mathrm{cyl,i}}(r_{\mathrm{i}} \leqslant r)\right) / M_{\mathrm{tot}}(\leqslant r), \tag{4}$$

where the most massive substructure is defined as the main and thus excluded. This fraction is projection dependent. It is worth noting that we primarily care for the value at the virial radius, and thus we define f_{cyl}, when it is given without an explicit radius, as the value at r_{vir}. Accordingly, the mass fraction contained within subhalos f_{sub} is calculated as the sum of all subhalos within the virial radius, excluding the most massive one, divided by the virial mass. This fraction is based on the full three-dimensional information—and as such, is a fixed quantity independent of projection. A comparison between both fractions is shown in Figure 3, with median values of f_{cyl} as a function of f_{sub}, colored by the mass bin of the galaxy cluster.

Generally, we find the projected masses to be larger, by a factor of around 2–3, than those determined from what is physically bound in local structures in three dimensions. As we also find little change with varying projection depth (see Appendix B), this is not primarily due to multiple galaxies being projected together into one aperture. Instead, this results from the main halo contributing to f_{cyl}. The scatter for individual galaxy clusters in f_{cyl} can vary by up to a factor of 2, as visible from the 1σ ranges. Overall, the more massive clusters like "giants" and "medium" tend to have larger substructure mass fractions (20%–30%). For these massive clusters, we find that the total projected substructure mass overestimates the amount of mass within self-bound subhalos by a factor of 3 on average. For the less massive clusters, the substructure mass is larger by a factor of 2. While this difference could be due to the fact that there is a higher number of substructures in those massive clusters compared to the smaller ones, it also cautions the interpretation of such signals from observations, as we find no difference in the f_{sub} values.

Another important characterization of galaxy clusters is the radial distribution of substructure masses. Figure 4 depicts the radial behavior of the substructure mass fraction f_{cyl}, where within a given radius r the summed substructure mass is divided by the total mass contained within this radius. The total mass here is comprised of the substructure mass plus the integrated main halo mass as given by the Einasto fit from Equation (2). At all radii and all cluster mass bins, we find that f_{cyl} is nearly constant for all four cluster mass bins, with fractions only dropping at radii below $0.2 \cdot r_{\mathrm{vir}}$. Between galaxy cluster mass bins, f_{cyl} increases with the mass of the galaxy cluster from the "tiny" to "medium" mass bin. Interestingly, f_{cyl} does not increase further to the most massive clusters, and instead it converges slightly below $f_{\mathrm{cyl}} = 20\%$.

We can also consider the impact of projection on the radial behavior of the subhalo mass fraction f_{sub} for the clusters of the "giants" mass bin in Figure 4 (nonsolid blue lines). Here, the bound subhalos from SUBFIND are treated as point-mass particles. They are then radially summed up and divided by the total mass within the radius. The dotted line shows this in 3D, and it generally lies the lowest, in particular toward the center, as there are very few bound subhalos at $r_{\mathrm{3D}} < 0.2 \cdot r_{\mathrm{vir}}$. In projection out to $1 \cdot r_{\mathrm{vir}}$ in front and behind the cluster center (blue dashed line), however, it is possible to have bound subhalos that simply *appear* close to the center but actually lie farther out. Correspondingly, the curve is much flatter toward the center. as here $x = r_{\mathrm{2D}}/r_{\mathrm{vir}}$ is instead the projected distance. Nonetheless, the values close to the virial radius converge to the 3D values, as the few additional subhalos within the corners of the projected cylinder compared to the sphere make no discernible difference. The radial subhalo mass fractions found for this kind of projection are comparable with those predicted by Jiang & van den Bosch (2017) from a dark matter only simulation set.

When projecting out to $r_z \approx 5 \cdot r_{\mathrm{vir}}$ (blue dashed–dotted line) the subhalo mass fraction is nearly indistinguishable from the projection out to $1 \cdot r_{\mathrm{vir}}$. The total mass fraction contained in bound subhalos at 10% thus still lies noticeably below the values we find when projecting the full particle distribution by around a factor of 2. Consequently, projection of bound subhalos alone is insufficient to explain the high substructure masses, and instead portions of their mass are the result of contributions from the main halo.

For comparison, the substructure mass fractions measured from lensing for the Coma cluster (Okabe et al. 2014, purple star) and A2744 (Jauzac et al. 2016, cyan diamond) are included in Figure 4. With respect to their masses, both are comparable to the "giants" mass bin (dark blue curve). Within the error bars, we find excellent agreement between our prediction and the observations, which is surprising given that A2744 has an extremely high fraction of mass in substructures

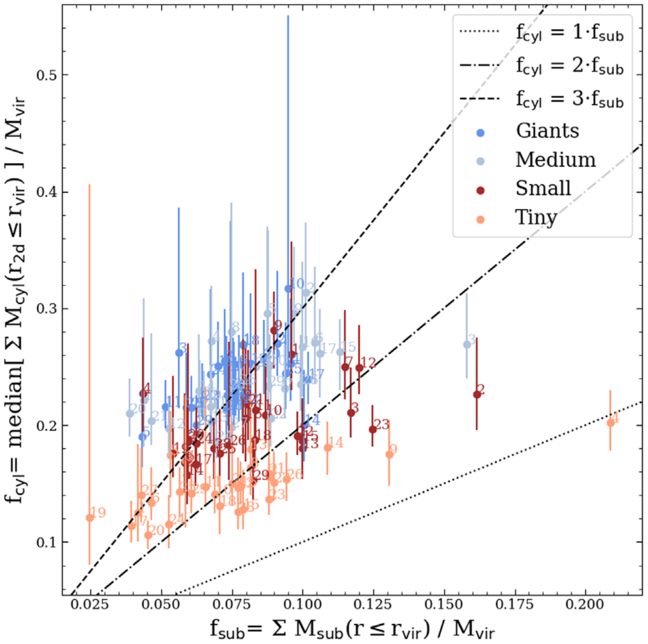

Figure 3. The median total substructure mass fraction f_{cyl} as a function of the total subhalo mass fraction f_{sub}, colored by the mass bin. Colored lines denote the 1σ range of f_{cyl}. The black lines denote respective factors of 1 (dotted), 2 (dashed–dotted), and 3 (dashed) between f_{cyl} and f_{sub}.

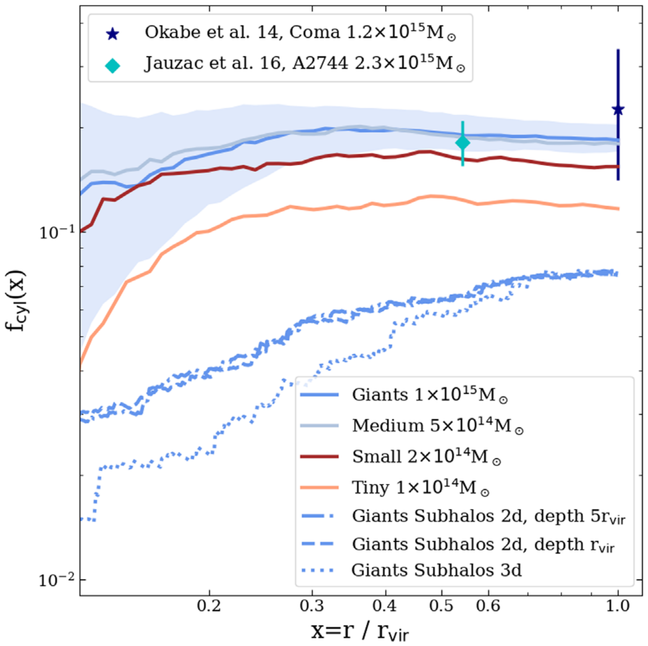

Figure 4. The radial dependence of the total mass within substructures as a fraction of total mass. For each mass bin (colored lines), the mean over all galaxy clusters is shown, where for the "giants" the 1σ range is additionally plotted (light blue area). Also shown for the "giants" is the radial behavior of the bound subhalo mass fraction f_{sub}, once in 3D (blue dotted) and once when projecting out to $1 \cdot r_{\mathrm{vir}}$ (blue dashed) and r_z (blue dashed–dotted). The cyan star and purple diamond represent values from lensing observations of the A2744 and Coma clusters, respectively, with vertical lines denoting the errors. For the 3D curve, x is the fractional 3D distance to the cluster center, while for all others, it is the fractional projected distance.

in comparison to other galaxy clusters. However, this could be due to the fact that only the amount of mass in the eight most massive substructures is considered here, neglecting all other smaller substructures. Adding more measurements in the future will enhance our understanding of typical substructure distributions in galaxy clusters.

4.2. Individual Substructure Masses

While on average the projection increases the total projected substructure mass relative to the total bound subhalo mass by around a factor of 2, the question arises of how strongly this scatters for individual measured substructures. In the following, we compare the individual projected masses to those of the bound subhalos within the same aperture. The majority of apertures contain just a single subhalo, though some can contain in excess of five. Defining the bound subhalo masses as $M_{\mathrm{sub,j}}$, then

$$M^{\mathrm{i}}_{\mathrm{sum\ sub\ in\ cyl}} \equiv \sum M_{\mathrm{sub,j\ in\ i}} \tag{5}$$

is the sum of all subhalos within an aperture i. In most cases, even when multiple subhalos are present, the total bound subhalo mass within an aperture is dominated by a single subhalo, where

$$M_{\mathrm{s}} \equiv \max\{M_{\mathrm{sub,j\ in\ i}}\} \tag{6}$$

is the mass of this most massive subhalo within the aperture.

Thus, Figure 5 shows the substructure mass M_{cyl} as a function of M_{s} for the four cluster mass bins in separate panels. All galaxy cluster mass bins exhibit very similar distributions, with the projected mass on average increasing with increasing subhalo masses. The scatter is much larger for subhalos of smaller masses, with the projected aperture masses spreading over multiple magnitudes for the lowest-mass subhalos. While we find that generally the mean substructure masses increase with the contained subhalo mass, the most massive substructure masses exhibit barely any dependence on the mass within the aperture, which is bound in individual subhalos, instead only very weakly increasing with M_{s}.

Assuming that a significant portion of this scatter in the $M_{\mathrm{cyl}} - M_{\mathrm{s}}$ correlation is caused by falsely adding contributions from the main halo, we should find a trend that those apertures closer to the center of mass experience stronger increases in M_{cyl}. This can indeed be seen in Figure 5, where the color encodes the projected distance of the center of the aperture to the center of mass normalized by the virial radius, $r_{\mathrm{2D}} \equiv (r_{\mathrm{cyl-CoM}})/r_{\mathrm{vir}}$. Apertures that are very close to the center of mass (colored blue) lie at consistently high substructure masses. Conversely, substructures far out (red) are very strongly dependent on M_{s}, following instead more the curvature of the solid gray curve.

This solid gray curve represents the mass within an aperture r_{ap} that would result from a single isolated halo that follows an NFW profile, with mass M_{s} and concentration following the concentration–mass relation from Ragagnin et al. (2019), when projected out to a depth r_z. This curve provides a lower bound to 95% of the substructures for all cluster mass bins, as can be seen from the contours. An upper bound on the other hand is given by the dashed gray line. This is determined in the same way as the solid curve, but for the most massive M_{s} within the cluster mass bin. Thus, it represents the substructure mass that one would get from projecting the center of the main halo, i.e., the highest-density area within the galaxy clusters.

The fact that the main bulk of substructure masses lie on or above the solid gray curve implies that the projected mass is in general *not* carried by a single subhalo. Instead, contributions

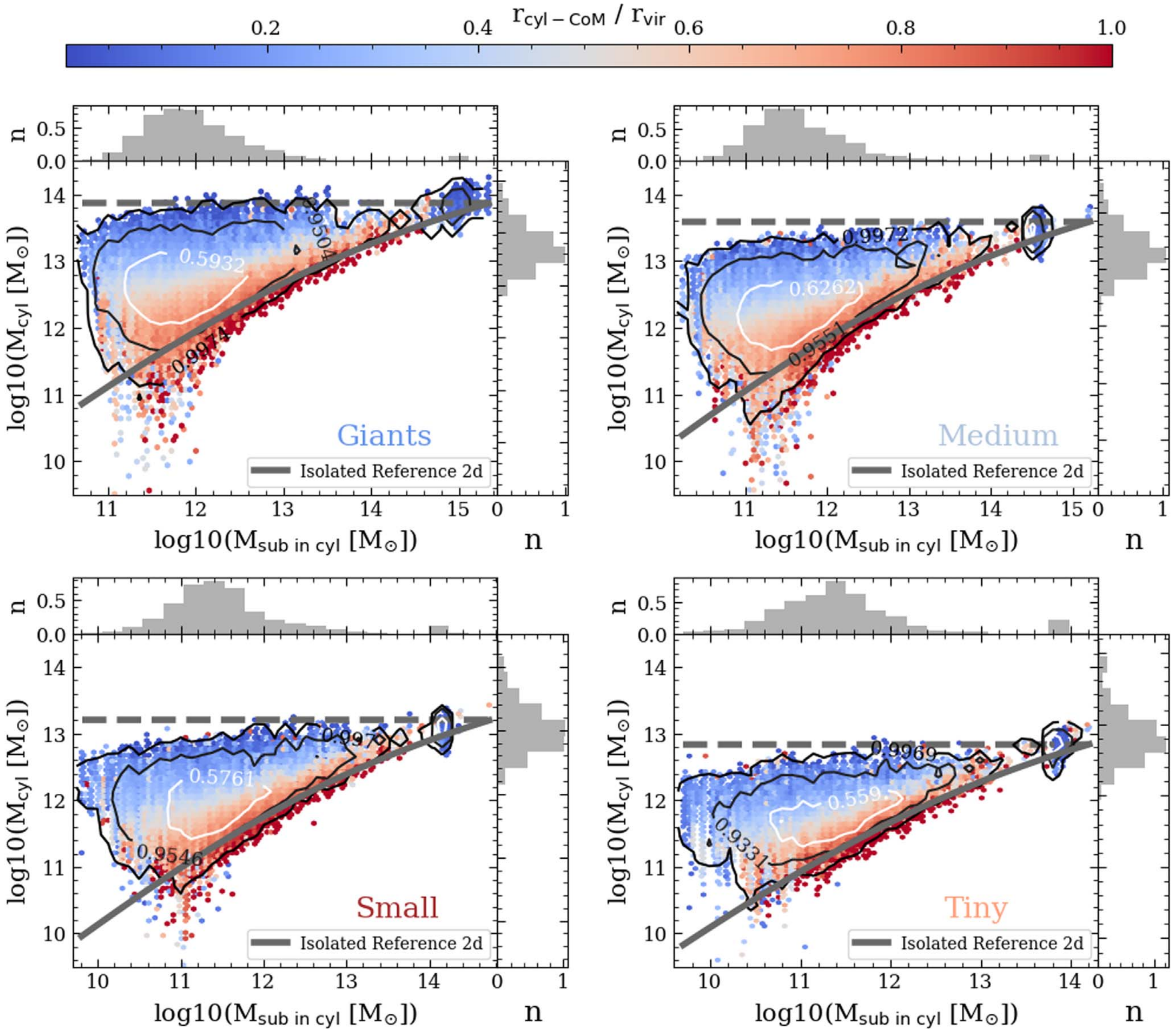

Figure 5. The substructure mass as a function of the associated subhalo mass for the four mass bins (as written), colored by the projected distance of the aperture to the center of mass. The solid (dashed) gray lines indicate the according cylindrical aperture mass for the equivalent (maximum) halo mass in isolation. See text for details. The contour lines contain the fraction of total substructures as written. Histograms depict the number density n distribution of either M_s (top) or M_{cyl} (right).

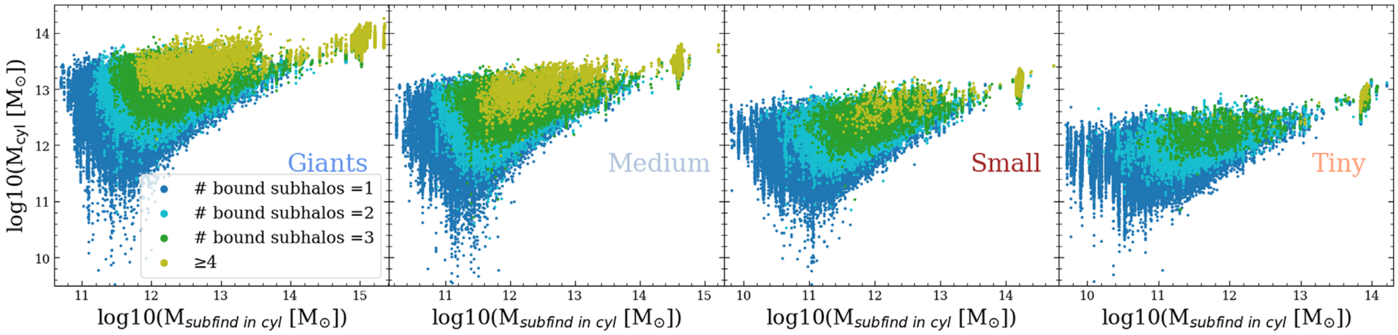

Figure 6. The substructure mass as a function of the most massive bound subhalo within its aperture as given by SUBFIND for the four mass bins (indicated within the plots), with colors denoting the number of bound subhalos within the substructures. The apertures containing a higher number of subhalos are plotted over those with less, to better show their behavior.

from the main halo in particular, as well as from other subhalos are relevant. The latter can be seen in Figure 6, where the substructures that contain higher numbers of subhalos are plotted over those with fewer. Those that contain these higher numbers are found in the top right of the $M_{\rm cyl} - M_{\rm s}$ plane, and thus they indicate substructures that are more massive. This, however, does not imply that all massive substructure must contain multiple subhalos, as there are apertures containing just one subhalo within the top right that are simply overplotted. Instead, the dependency on projected distance seen in Figure 5, and thus the main halo contribution, is more significant to the final substructure mass, with the number of included subhalos being a secondary effect.

4.3. *Quantifying* $\mathrm{M}_{cyl} - \mathrm{M}_{s}$

Based on the strong radial dependence as $M_{\mathrm{cyl}} = M_{\mathrm{cyl}}(M_{\mathrm{s}}, r_{\mathrm{2D}})$, it is possible to construct a predictor function for the range of projected substructure masses that can arise for a given bound mass at a given projected distance to the cluster center. The parameter space is split into $n \times m$ bins in M_{s} and r_{2D}. Within each bin, the distribution of substructure masses M_{cyl} follows a Gaussian (see Figure 14 in the appendix for an example):

$$f(x = M_{\mathrm{sub}};\, \mu, \sigma) = \frac{1}{\sqrt{2\pi\sigma^2}} \cdot \exp\left\{-\frac{(x-\mu)^2}{2\sigma^2}\right\}, \tag{7}$$

indicating that other possible systematics are comparatively minor (as the Gaussian represents a random distribution). This holds true so long as the number of bins is sufficiently high, $(n, m) \geqslant 10$, as a low number of bins smears many different substructures over each other, resulting in a distribution that is instead comprised of a sum of Gaussians. Here, $(n, m) = (50, 50)$ is chosen throughout.

The fit parameters of the Gaussian are then the mean $\mu(M_{\mathrm{s}}, r_{\mathrm{2D}})$ and variance $\sigma(M_{\mathrm{s}}, r_{\mathrm{2D}})$. We find that the variance does not depend strongly on the projected distance, and it is fit best by the form

$$\sigma(M_{\mathrm{s}}) = \gamma \cdot \log_{10}(M_{\mathrm{s}}[M_\odot]) + \sigma_0. \tag{8}$$

This can be seen in Figure 5, as the scatter is mainly dependent on M_{s}, with substructures containing low-mass subhalos scattering strongly in M_{cyl} while those with higher M_{s} scatter less, regardless of the projected distance. Consequently, $\gamma < 0$.

As for the means μ, one can consider a bin in r_{2D}, for example $r_{\mathrm{2D}} < 0.2$. Substructures located at these distances will primarily occupy the dark blue regions in Figure 5. Splitting this region into M_{s} bins (and thus vertical slices in Figure 5) and determining the means μ finds them weakly linearly increasing in logspace with M_{s}, so

$$\log_{10}(\mu) = \alpha \cdot \log_{10}(M_{\mathrm{s}}[M_\odot]) + \beta, \tag{9}$$

with $\alpha, \beta > 0$. If considering the same for a bin of larger r_{2D}, for example the dark red region, then the slope becomes larger and the y-intercept decreases. This dependency of a, b on the projected distance can be fit well by a line, such that

$$\alpha(r_{\mathrm{2d}}) = \alpha_{\mathrm{r}} \cdot r_{\mathrm{2d}} + \alpha_0, \tag{10}$$

$$\beta(r_{\mathrm{2d}}) = \beta_{\mathrm{r}} \cdot r_{\mathrm{2d}} + \beta_0, \tag{11}$$

with $\alpha_{\mathrm{r}} > 0$ and $\beta_{\mathrm{r}} < 0$. It is worth noting that α_0 describes the distance-independent relationship between $\mu - M_{\mathrm{s}}$ and is thus expected to be positive, while β_0 is the overall y-intercept of the line fits and thus should be on the order of typical values of μ.

Combining Equation (9) with Equations (10) and (11) gives the mean substructure mass as a function of projected radius and bound mass as

$$\log_{10}(\mu(M_{\mathrm{s}}, r_{\mathrm{2d}})) = (\alpha_{\mathrm{r}} \cdot r_{\mathrm{2d}} + \alpha_0) \cdot \log_{10}(M_{\mathrm{s}}[M_\odot]) + \beta_{\mathrm{r}} \cdot r_{\mathrm{2d}} + \beta_0. \tag{12}$$

Table 3

Summary of the Predictor Function Parameters for the Four Mass Bins

Mass Bin	γ	σ_0	α_{r}	α_0	β_{r}	β_0
Giants	−0.0683	1.05	0.231	0.206	−3.76	10.8
Medium	−0.0666	1.01	0.218	0.226	−3.42	10.2
Small	−0.0557	0.834	0.250	0.216	−3.72	9.96
Tiny	−0.0548	0.789	0.323	0.210	−4.43	9.80

The resulting parameters for the Gaussians are then two for the variance (γ, σ_0), and four for the means (α_{r}, α_0, β_{r}, β_0). They are summarized for the different mass bins in Table 3.

Using these parameters allows to predict the distribution of possible projected substructure masses that result from some bound subhalo of mass M_{s} located at projected distance r_{2D} from the projected center of mass. It should be noted that these parameters vary with different masses of the host galaxy cluster (i.e., between cluster mass bins). The ratio of predicted mean mass of each substructure, $\mu \equiv M_{\mathrm{calc,cyl}}$, to actual measured mass M_{cyl} is plotted in Figure 7. Around 80% of substructure masses are predicted within a factor of 2 of their real values, as highlighted in gray.

In summary, we find that, on average, the projected substructure masses within apertures of a given size are about a factor of 2–3 larger than the masses that are actually bound in subhalos, for all cluster mass ranges. Furthermore, the radial distance to the cluster center plays a crucial role in the amount of additional mass added to the individual substructures, in that substructures closer to the center may contain matter from the main halos that did not get perfectly subtracted. Moreover, some apertures can also contain more than one subhalo, adding to the overestimate of the mass. We provide a predictor function for future comparison studies between simulations and observations for the mass contained inside a substructure calculated from the subhalo mass and its distance from the main halo center that allows to predict the expected overestimate of the mass in projection without actually having to go through the process of projecting the cluster from simulations. We conclude that it is necessary to take into consideration projection effects—but especially the fact that observationally it is not possible to separate bound from unbound material when comparing simulations and observations, to ensure a fair comparison.

5. Substructures and Cluster Dynamical State

The existence of multiple massive substructures inside a galaxy cluster is thought to be connected to recent merging activity. For example, this is discussed by Jauzac et al. (2016) for the case of the galaxy cluster A2744, which is especially well known for its multiple massive substructures. Therefore, we will test this hypothesis in the following by first reproducing A2744 from the simulations, using the method described in Section 3 to account for the projection effect, and then tracking its formation pathways. Furthermore, we then broaden the analysis to our full cluster sample, aiming to encode the information hidden in these substructures.

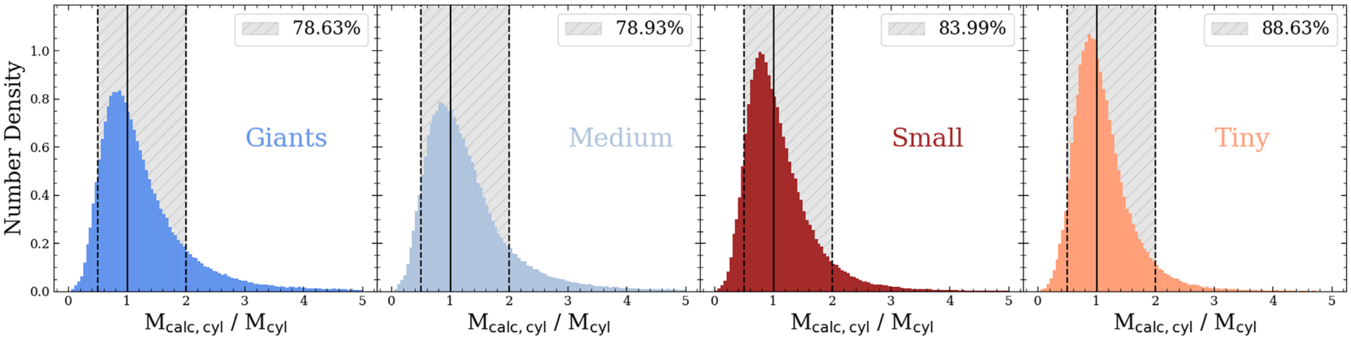

Figure 7. The distribution of ratios between predicted $M_{\rm cal,cyl}$ to measured substructure mass $M_{\rm cyl}$, for each of the four mass bins (indicated within the plots). The prediction is made via Equation (12) and the parameters from Table 3. The solid vertical black line denotes equality, with the gray shaded area enclosing those within a factor of 2, with the number of substructures predicted within this range given in the legends.

5.1. The Case of Abell 2744

Using gravitational lensing measurements, Jauzac et al. (2016) found extremely large masses inside substructures for the galaxy cluster A2744, significantly more than can be found within simulations (Schwinn et al. 2017). Using dark matter only simulations, Mao et al. (2018) and Schwinn et al. (2018) present evidence that the discrepancy is caused by projection effects. Here, we will use, for the first time, a fully baryonic hydrodynamic cosmological simulation to identify A2744 counterparts, applying the method outlined in Section 3.

The eight substructures found by Jauzac et al. (2016) within A2744 are not only very massive but also in close proximity within 1 Mpc. They find that the eighth-most massive substructure still has a mass of $M_{\rm cyl,8} = 5 \times 10^{13} M_\odot$ within an aperture of $r_{\rm ap} = 150$ kpc (see Table 4). When compared to their measurement of the total mass within a radius $r_{\rm tot} = 1.3$ Mpc, $M_{\rm tot} = 2.3 \times 10^{15} M_\odot$, this is still equal to around 2.17%. Using the method from Section 3, we find a total of 58 projections of galaxy clusters from the "giants" mass bin that manage to reproduce eight extremely massive substructures with a mass fraction $M_{\rm cyl}/M_{\rm tot} > 2.17\%$. It is worth noting that $M_{\rm tot}$ is defined here as the total projected mass within 1.3 Mpc, to be comparable to the results by Jauzac et al. (2016).

The case that best reproduced the measurements for A2744 is a projection of galaxy cluster number 20 from the "giants." The central $(2\ {\rm Mpc})^2$ region of the best projection is shown in Figure 8. As seen on the top left, the eight most massive substructures (black circles) all lie close to the center (black x) and follow a strongly elongated distribution. For comparison, the stellar surface density (bottom left) as well as a mock image in the r band (bottom right) are shown. The black numbers are sorted by the mass of the substructures. Their mass as a fraction of $M_{\rm tot}$ is shown on the top right, with the values for this projection denoted as red crosses while the eight substructures observed in A2744 by Jauzac et al. (2016) are shown as cyan diamonds. We find an exceedingly similar flat distribution of substructure mass fractions aside from the most massive one, in excellent agreement with the observations. This agreement can also be seen from the mass fractions of the individual substructures as shown in Table 4.

While this is the best-fitting projection, it is not the only one, as can be seen from the shaded areas for each substructure in the upper right panel of Figure 8: Underlaid in blue is the distribution of substructure masses for all 200 orientations of galaxy cluster 20, with the size of the bulge corresponding to the relative frequency of each value. The overall spread between orientations (blue vertical lines) is sizable. It can be concluded that, while the extreme mass distribution within A2744 is reproducible, it represents an outlier, with very high substructure mass fractions for the fifth to eighth substructures.

Table 4
Substructure Mass Comparison A2744–Cluster 20

ID	1 Core	2 NW	3 S3	4 N	5 S4	6 S2	7 $W_{\rm bis}$	8 S1
				Mass Fraction [%]				
A2744	5.9	3.4	2.8	2.7	2.4	2.3	2.3	2.2
Cl20	3.6	3.5	2.6	2.6	2.6	2.3	2.2	2.2
				Total Masses of Structures [$10^{13} M_\odot$]				
A2744	13.55	7.9	6.5	6.1	5.5	5.4	5.2	5.0
Cl20	3.7	3.7	2.7	2.7	2.7	2.4	2.3	2.3

Notes. The eight substructure masses determined within 150 kpc apertures for a projection of galaxy cluster 20 of the "giants" as well as A2744, with values for the latter as determined by Jauzac et al. (2016).

This means that the masses observed in A2744 are reproducible within simulations also when including baryons, and they arise from projection effects. The impact from projection becomes especially clear when considering the orange points in the upper right panel of Figure 8. These mark the subhalo mass fractions as determined by SUBFIND, i.e., when only counting the matter to the structure that is really bound to it. In this case, only the first and second subhalos have mass fractions comparable to the *eighth* substructure within A2744, with all other subhalos lying far below. The mass fraction of the first subhalo lies much higher outside of the plotted range, as it is the main halo and thus assigned all bound mass of the galaxy cluster not within other subhalos. This clearly highlights the difficulty in comparing substructures obtained from simulation algorithms and observations: accounting not just for projection effects but also for the impossibility of separating bound from unbound structures in observations.

As outlined by Jauzac et al. (2016), one of the eight measured substructures, $W_{\rm bis}$, is most likely a background source. When excluding the potential background source $W_{\rm bis}$, the number of projections of galaxy clusters from the "giants" mass bin with seven substructures of mass $M_{\rm cyl}/M_{\rm tot} > 2.17\%$ rises to 108. However, the projections made here go out to a depth of $r_z \approx 5 \cdot r_{\rm vir}$. We can instead require all the

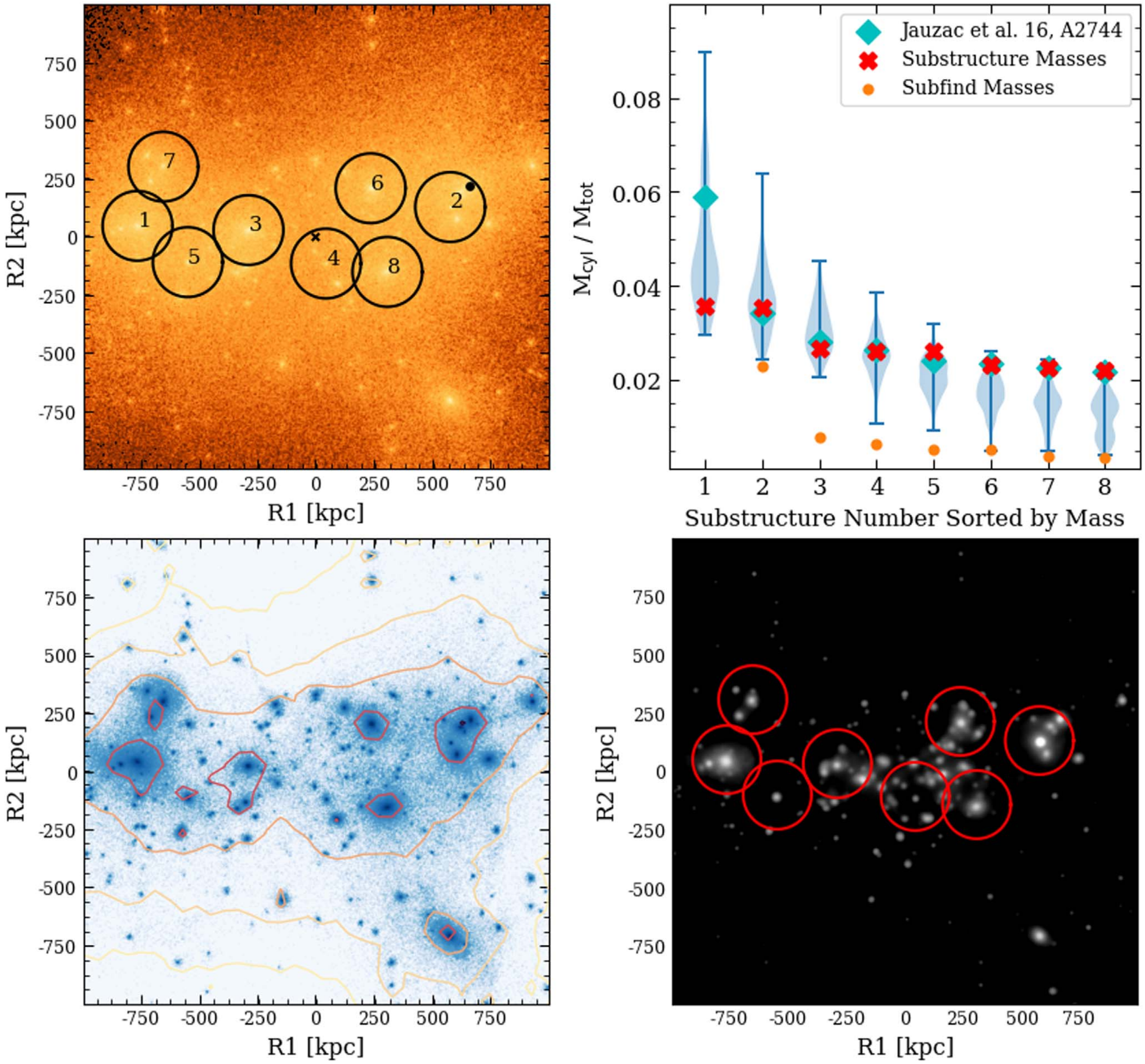

Figure 8. Top left: surface mass density map of the central (2 Mpc)^2 region of galaxy cluster 20 of the "giants" for the best projection found overall, centered on the projected center of mass (black cross) with the SUBFIND cluster center indicated as a black dot. The redshift is $z = 0.252$. The eight most massive substructures are shown as black circles numbered in decreasing order of mass. Top right: the substructure masses as a fraction of the total mass for the best projection (red crosses) as compared to those in A2744 (blue diamonds) determined by Jauzac et al. (2016). Underlaid in blue is the total distribution of masses for all 200 random projections of the galaxy cluster, with the width of the shaded area denoting their relative frequency. The subhalo masses from SUBFIND (orange dots) are given as a fraction of the $M_{\rm tot}$ for the best projection. Bottom left: same as top left, but for the stars, with isodensity contours from the total mass map overlaid. Bottom right: mock image in the r band as seen from $z = 0$ down to a limiting magnitude of 25 mag, generated via the method from Martin et al. (2022). The red circles denote the eight most massive identified substructures. Colorbar ranges for the surface density maps are the same as in Figure 1.

substructures to not be background sources by projecting out only to a depth of $1 \cdot r_{\rm vir}$. Therefore, we repeated the study for 200 orientations of the cluster that provided the best reproduction of A2744, namely galaxy cluster 20. In this case, we find 15 projections with seven substructures of mass $M_{\rm cyl}/M_{\rm tot} > 2.17\%$ (and even two with eight). We conclude that A2744 can still be reproduced well by galaxy cluster 20, even if only substructures inside the galaxy cluster virial radius are considered. A comparison between these different projection depths for "giant" clusters 5 and 20 is discussed in detail in Appendix B.

It should be noted that the reported virial radius and mass of A2744 by Schwinn et al. (2017) are approximated by the radius enclosing 200 times the critical density, $r_{200} = 2.8$ Mpc and $M_{200} = 3.3 \times 10^{15} M_\odot$. They are larger than the corresponding values for, e.g., cluster 20 of $r_{200} = 2.0$ Mpc and $M_{200} = 1.1 \times 10^{15} M_\odot$. For the best projection in particular, $M_{\rm tot} = 1.03 \times 10^{15} M_\odot$ for cluster 20 while $M_{\rm tot} = 2.3 \times 10^{15} M_\odot$ for A2744. Given the generally constant or increasing substructure mass fraction with increasing galaxy cluster mass from Figure 4 and the self-similarity of the subhalo mass functions of all our galaxy cluster bins from

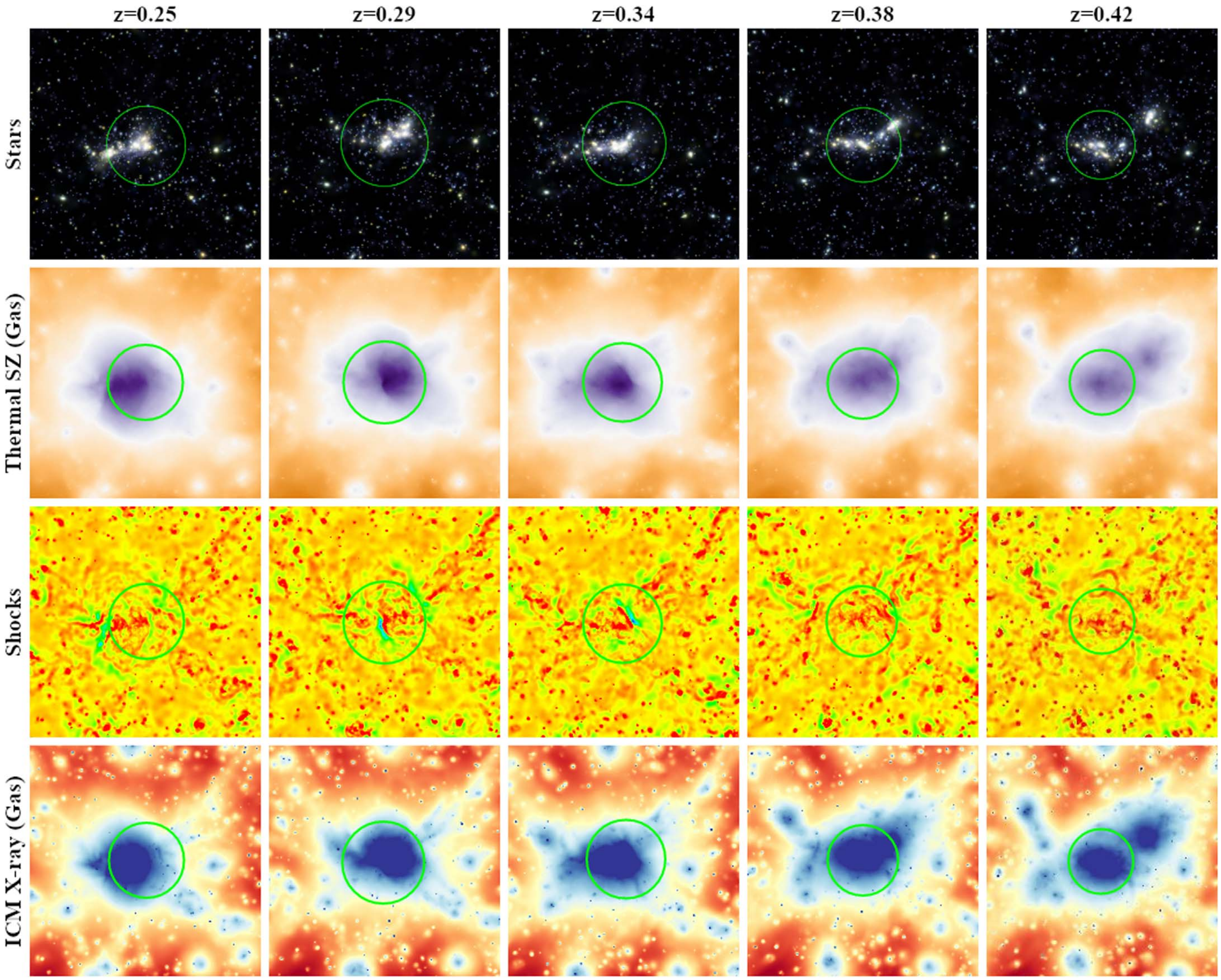

Figure 9. Redshift evolution of cluster 20 of the "giants," the A2744 counterpart, with the different columns showing the different redshifts as indicated in the column titles. In all panels, the green circle marks the R_{500} radius of the cluster as calculated from the 3D mass distribution at each redshift. For scaling, at $z = 0$, this corresponds to $R_{500} = 1.94$Mpc. Top row: stellar components. Second row: maps of the thermal SZ effect, shown as Compton-X maps, with color according to the thermal pressure from low (orange) to high (violet). Third row: shocks calculated from the Compton-X maps, with shocks in green or even blue if strongly compressed. Bottom row: X-ray emission from the hot gas component, from low (red) to bright (dark blue).

Figure 2, it would stand to reason that a larger box would also be able to reproduce A2744 with comparable absolute substructure masses. This is supported also by the fact that galaxy clusters of a total mass comparable to A2744 are found in the larger volume of the Magneticum Pathfinder simulation suite (see Figure 15 of Remus et al. 2022); however, the resolution of that simulation is too low for a substructure study as performed in this work.

It should be further noted that we selected galaxy cluster 20 at $z = 0.252$ to better match the state of post-core passage claimed for A2744. As we discuss in more detail in the following, at $z = 0.29$, cluster 20 is in the middle of the first passage of the most massive merger. As the true state of A2744 is most likely matched by the configuration in between the two simulation snapshots, we have chosen the snapshot farther in the post-core passage phase. We do not expect a large difference when using the other, as there is no significant additional matter infall between the two snapshots (as shown in Figures 9 and 10).

The similarities in the substructure masses found for galaxy cluster 20 of the "giants" to A2744 motivate a closer look at their origin. Figure 9 shows the evolution of galaxy cluster 20 from $z = 0.42$ (right column) to $z = 0.25$ (left column), in maps depicting the stars, thermal SZ emission from the gas, the corresponding shocks, and finally the X-ray emission (top to bottom row). The images are centered on the deepest point of the potential at each time, while the green circle denotes r_{500}.

In the stellar maps, we see that galaxy cluster 20 is the result of a recent major merger with a mass ratio of 1:1.4. The initial two clusters are visually distinct for $z = 0.42$, where one is centrally located and the other lies to the upper right, immediately outside r_{500} (henceforth cluster "A" and "B"). B has been on an infalling trajectory since $z = 0.67$ but has just reached a distance of $r_{3D} = 1.68$ Mpc at $z = 0.42$. Even though it is already within the $r_{200} = 2.15$ Mpc of cluster A at this time,

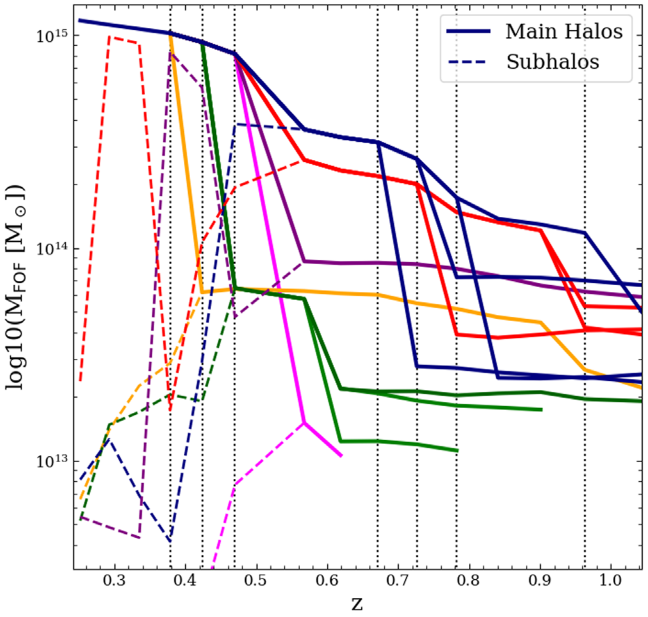

Figure 10. Merger history of A2744 counterpart cluster 20 of the "giants," with main halos (solid) and their respective subhalos after infall (dashed lines). Subhalo masses are the summed mass of all bound particles. Only main halos with masses $M_{\rm FOF} \geqslant 1 \times 10^{13} M_\odot$ are shown. Branches belonging to the two components A and B of the major merger are in blue and red, respectively.

SUBFIND still assigns it a mass of $M_{\rm sub,B} = 1.1 \times 10^{14} M_\odot$. Moving forward in time, cluster B falls within r_{500} of A at $z = 0.38$, such that a significant portion of its mass is now assigned to cluster A, with $M_{\rm sub,B}$ dropping to $1.7 \times 10^{13} M_\odot$. This coincides with a connection of regions of high X-ray emission from the hot gas halos, as can be seen in the bottom row, going from two distinct peaks to one.

Moving to $z = 0.34$, the nearly radial infall of cluster B triggers a strongly peaked shock (see third row of Figure 9) to the immediate upper right of the cluster center of cluster A. As cluster B re-emerges toward the bottom left at $z = 0.29$ and then continues left until $z = 0.25$, the shock front is pushed along. This is in excellent agreement with observations of shock fronts observed in A2744 in X-ray with Chandra by Owers et al. (2011), coinciding with radio relics (Eckert et al. 2016; Rajpurohit et al. 2021). These shock fronts have been interpreted to result from a post-core-passage major merger with a resulting shock front toward the southeast (see also Kempner & David 2004; Boschin et al. 2006), exhibiting much the same characteristics found here for galaxy cluster 20.

Following the evolution of cluster 20 further back in time as shown in Figure 10, we find that it actually only assembled to a mass above $M_{\rm FOF} \geqslant 1 \times 10^{14} M_\odot$ at about $z \approx 0.96$. It is the result of multiple group merger events happening simultaneously: between $z = 0.62$ and $z = 0.42$, four halos with masses above group mass (i.e., $M_{\rm FOF} \geqslant 1 \times 10^{13} M_\odot$) are accreted onto the main halo A in addition to cluster B, with mass ratios relative to cluster A at the time of merging of about 1:4, 1:6, 1:6, and 1:24. We note here that, different than the case for galaxies, a 1:24 merger is still a massive merger event in case of galaxy clusters. This is because the 1:24 merger is a group being accreted onto the cluster, which, by itself, already harbors several galaxies and a hot gaseous halo. This supports claims from observations that A2744 actually originated not only from a single major merger but rather several ongoing multiple merger events (e.g., Merten et al. 2011; Rajpurohit et al. 2021). Indeed, we find that, of the total growth in mass from $z = 0.67$ to $z = 0.25$, 58% comes from mergers with halos of mass larger than $1 \times 10^{13} M_\odot$. This means that, for the case of cluster 20, a significant amount of the mass of the cluster is pre-processed in groups.

Finally, the lower row of Figure 9 clearly shows that cluster 20 is fed through four filaments, which are especially visible at $z = 0.29$ and $z = 0.34$. This supports the idea that the multiple filaments observed by Eckert et al. (2015) in the hot gas map constructed for A2744 using XMM-Newton data could be depicting four feeding filaments surrounding the cluster. All this gives further evidence that cluster 20 from the *Magneticum* simulation indeed resembles A2744. We conclude that A2744 is indeed a rare case of a violently assembling galaxy cluster, sitting at a node in the cosmic web that only recently started to collapse from multiple different directions.

5.2. Accretion and Dynamical State

Given the flat distribution of the mass fractions of the substructures for both A2744 and our cluster 20 (see upper right panel of Figure 8), the mass fraction of the eighth substructure is still rather large. As we have seen, our best-matching cluster to Abell 2744, cluster 20, is highly dynamical, active, and dominated by recent multiple accretion events. Thus, the question arises of how effective the mass fraction of the eighth substructure would be in tracing the recent assembly history of a cluster, independent of the galaxy cluster mass.

To this end, we calculate for each cluster in our four cluster mass bins the median mass fraction of the eighth substructure from all projections, f_8. The first column of Figure 11 depicts the mass accretion histories of the galaxy clusters of the "giant," "medium," and "small" cluster mass bins, respectively. More explicit, the mass fraction of the final cluster mass (at $z = 0.252$) is shown as a function of redshift. All individual clusters are shown as gray lines, with the three clusters with the highest f_8 for each cluster mass bin shown in blue, and those three with the lowest f_8 marked in red.

As can be seen immediately, for all cluster mass bins, the clusters with the lowest f_8 show relatively flat recent accretion histories. This means that only small amounts of mass are accreted in at least the last 2 Gyr, while all clusters with the highest f_8 have accreted at least half of their mass in the last 2 to 3 Gyr. To be more specific, for the "giants," we find that the three galaxy clusters with the highest f_8 have gained around 55 to 68% of their final mass starting from $z \approx 0.47$ (equaling around 2 Gyr). This is significantly enhanced recent accretion activity compared to 17%–31% for those with the lowest f_8. This shows that the relative mass of the eighth substructure is a good indicator for the amount of accretion in the last 2 Gyr, as large values in f_8 can only be reached through recent large mass infall, with a high likelihood for a major merger event.

Given that the mass fraction of the eighth substructure is to first order an arbitrary choice, we also tested the correlation between the recent mass accretion history with the mass fractions of the fourth, fifth, and sixteenth substructure mass fractions f_4, f_5, and f_{16}. While the split is surprisingly the clearest for the eighth substructure fraction f_8, both f_4 and f_5 give similarly good results, while the signal vanishes when using the sixteenth substructure mass fraction. We also inspected the properties found for the second-most massive substructure, but the connection to the mass history was less clear. This indicates that a single merger in the recent accretion

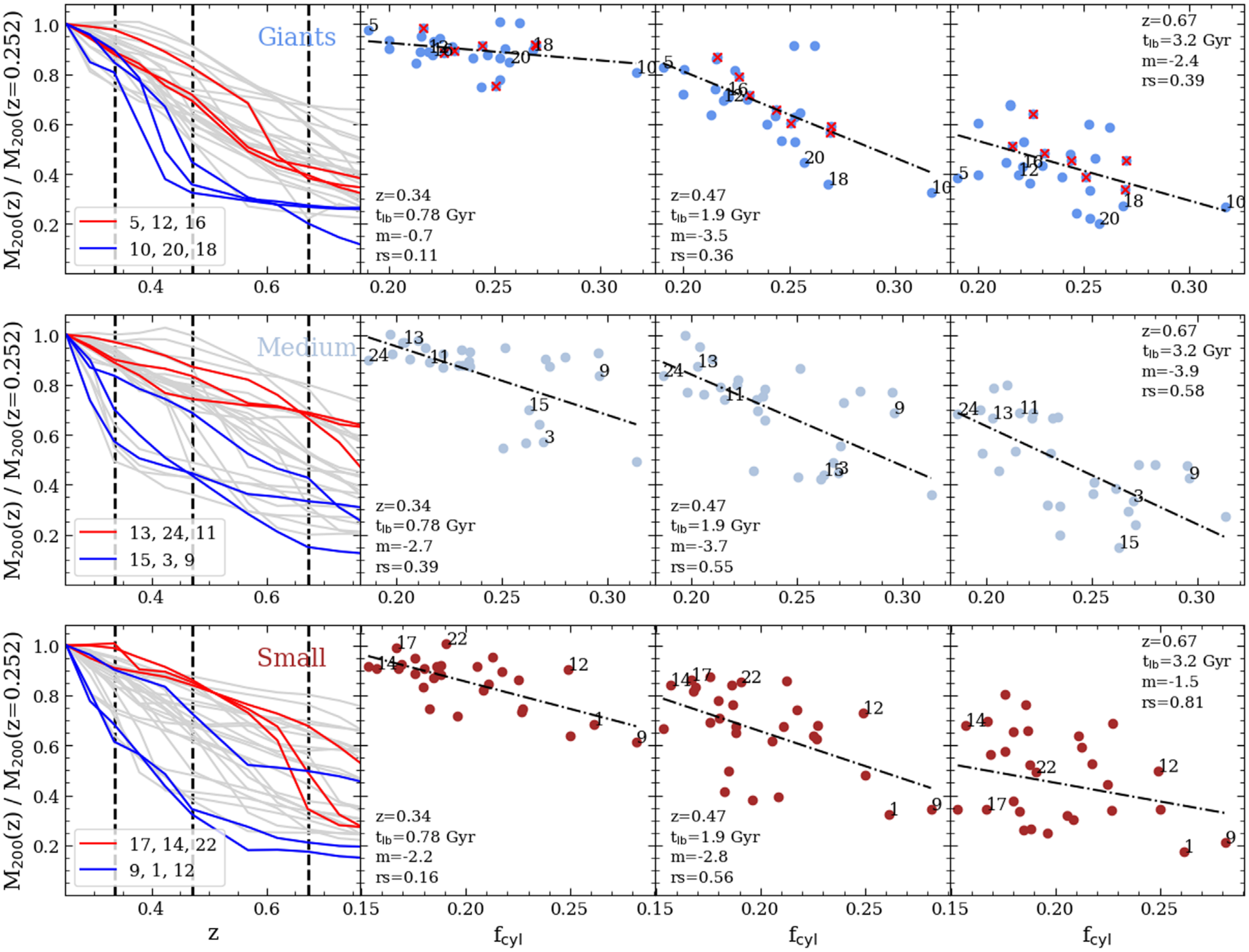

Figure 11. The mass history of the galaxy clusters of the "giant" to the "small" mass bins (top to bottom row) as a function of redshift (*first column*). The three galaxy clusters with the highest (lowest) f_8 are highlighted in blue (red), with their numbers given in the legend, and the three vertical black lines indicate three redshifts ($z = 0.34$, 0.47, 0.67). For each, the mass fraction of the final mass of the clusters is depicted as a function of $f_{\rm cyl}$ (*second to fourth column*), and the black dashed–dotted line is the best fit to the points. The slope m and residual rs of the fit are given in the legend. $t_{\rm lb}$ is the lookback time from the final redshift $z = 0.252$. Numbers indicate the six highlighted clusters, while the red crosses for the "giants" indicate galaxy clusters that were classified as protoclusters at $z = 4$ by Remus et al. (2022).

history of a cluster leading to a single massive remaining substructure does not necessarily trace a violent multiple merger dominated mass accretion history; rather, it is simply an event that occurs for any cluster (see Ragagnin et al. 2019, for more details on the mass ratio of the second-most massive substructure and the so-called fossilness parameter).

To avoid picking a single substructure to trace the mass accretion history, one can also use the total mass fraction contained within substructures $f_{\rm cyl}$ as a tracer for the dynamical state of a galaxy cluster. Previous studies found that higher values of $f_{\rm cyl}$ indicate a dynamically active galaxy cluster (De Lucia et al. 2004; Neto et al. 2007; Biffi et al. 2016). This is because, once a subhalo falls into a larger halo's influence, it begins being disrupted by processes such as ram pressure and tidal stripping. Given that the accretion of new subhalos is slower than the disruption at lower redshifts (Jiang & van den Bosch 2016), this leads to a net reduction of $f_{\rm cyl}$ with time—and consequently, a higher $f_{\rm cyl}$ correlates with a more recent formation time, as described by Jiang & van den Bosch (2017).

While using $f_{\rm cyl}$ is not as efficient as f_8 in identifying the extremes of the dynamically active or passive clusters, we find it to be an overall excellent tracer for the recent mass accretion history. To more closely quantify the relation between final substructure mass and the mass accretion history, we select three redshifts as indicated by the vertical black lines in the left panels of Figure 11. We then plot the mass fractions of the final masses of the clusters at these redshifts as a function of the final substructure mass fraction $f_{\rm cyl}$ in the three right columns of Figure 11.

For the first at $z = 0.34$, all clusters have only accreted a little mass, with a negligible dependence on $f_{\rm cyl}$. This can also be seen from the shallow slope m of the best-fit line (black dashed–dotted) given in the legend. Going further back to $z = 0.47$, however, shows a steep trend toward decreasing mass fraction with increasing $f_{\rm cyl}$. This means that galaxy clusters exhibiting high substructure masses are indicative of a large amount of recent (within 2 Gyr) mass accretion. This trend persists (although with a more shallow slope) out to $z = 0.67$, with a comparable scatter as indicated by the residual of the fit (given as rs).

The same correlation between the total mass fraction in substructures $f_{\rm cyl}$ and the cluster mass accretion history can be found for all galaxy cluster mass bins as shown in Figure 11 ("giants": upper row, "medium": middle row, and "small": bottom row), with two notable exceptions. First, the less massive galaxy clusters already show a noticeable slope at $z = 0.34$, though this is likely due to none of the clusters of the "giants" having accreted as high a mass fraction within the same period. Second, the scatter in the relation is higher at $z = 0.67$ for the "medium" and "small" galaxy clusters compared to the "giants," as can be seen from the fit residual. Nonetheless, we still find a downward slope present. It follows that the final substructure mass fraction measured in projection $f_{\rm cyl}$ is still a tracer for the mass accretion history, even out to a lookback time of $t_{\rm lb} = 3.2$ Gyr. This time period is larger than the mass-loss timescale of subhalos as given by Jiang & van den Bosch (2017) for dark matter only halos, which may indicate that the presence of baryons allows the signal to persist for longer. We conclude that a large substructure mass fraction $f_{\rm cyl}$ is an excellent tracer for a large amount of accretion within the last 2 Gyr and can be indicative of recent major merger events. Furthermore, large values of $f_{\rm cyl}$ hint at more merger events happening at even earlier times, without the corresponding stellar cores of these structures being disrupted.

Additionally, the red crosses in Figure 11 at all three redshifts of the "giants" indicate galaxy clusters that were classified as protoclusters at $z = 4.2$ by Remus et al. (2022). These are galaxy clusters for which their progenitor had already assembled at least a mass of $M_{\rm vir} \geqslant 1 \times 10^{13} M_\odot$ at $z = 4.2$, i.e., they are nodes that started collapsing early on. Interestingly, fulfilling various conditions to be a protocluster at high redshifts (for example, having a high star formation rate, high number of substructures, or being very massive) is found here not to correlate either with a particularly high or low resulting substructure mass fraction $f_{\rm cyl}$, nor with noticeable deviations from the best-fit lines. Instead, those clusters that started collapsing early behave here comparably to those that had not yet started to collapse and build up into a protocluster at $z \approx 4$. This clearly indicates that neither the mass nor the activity of assembly (i.e., the substructure mass fraction $f_{\rm cyl}$) observed at low redshifts is an indicator for the cluster having already assembled a significant amount of its mass at high redshifts. In fact, this is in agreement with our results for cluster 20, the A2744 analog, that we found to have assembled only recently below $z = 1$ even though it is one of the most massive galaxy clusters in our simulation volume. Furthermore, only about 25% of our most massive galaxy clusters are identified as protoclusters at redshifts of $z \approx 4$. Nevertheless, we do find one trend for the seven protoclusters present in our sample: the four protoclusters selected by their high number of substructures at $z \approx 4$ are also those that result in a higher $f_{\rm cyl}$ compared to the other three selected by mass or star formation rate. This could indicate that these particular clusters sit at large nodes of the cosmic web, building up into future super clusters; however, we note that the sample here is of low significance, due to the small number of clusters.

5.3. Substructures and Centershift

Another parameter that, according to the literature, correlates to the dynamical state of a galaxy cluster is the centershift s. It is defined as the distance between the point of lowest potential (highest density) to the center of mass (Biffi et al. 2016). As with $f_{\rm cyl}$, a higher centershift s indicates a dynamically active galaxy cluster, and the absolute value is typically divided by the virial radius to allow for comparisons between galaxy clusters of varying masses and sizes. Generally, thresholds of $f > 0.1$ and $s > 0.07$ are defined to be indicative of dynamical activity (Neto et al. 2007). However, the large differences between the total substructure mass fraction in projection $f_{\rm cyl}$ and the total subhalo mass fraction in three dimensions $f_{\rm sub}$ found in Figure 3 cause problems when consistently classifying the dynamical state in observations and simulations. Thus, in the following, we will investigate the importance of projection effects and the neglect of a binding criterion as used in three-dimensional substructure identifications for using f and s as tracers of dynamical activity.

Figure 12 shows in the first two rows the median projected values of f and s as a function of their three-dimensional values, with the thresholds for dynamical activity from Neto et al. (2007) given as dashed lines. Although we find a trend of increasing $f_{\rm cyl}$ with increasing $f_{\rm sub}$ in the top row, the projected values of $f_{\rm cyl}$ all lie above the threshold even when their values of $f_{\rm sub}$ are lower than the threshold. This would necessitate either an increased threshold in projection or a decreased threshold in three dimensions in order to agree when predicting dynamical activity.

Conversely, the centershift is found to agree well between projection and three dimensions. Overall, the number of clusters whose dynamical state would be classified the same between two to three dimensions is found here to be 18 of 116 when using f as a tracer, compared to 103 of 116 when using s (or around 15.6% versus 88.8%).

Given that the centershift is a consistent determinant for the dynamical state, independently of whether it is measured from projections in observations or intrinsically from simulations, the question is how well it correlates with $f_{\rm cyl}$. We indeed find a good agreement, in that high centershift corresponds to high substructure masses, as shown in the bottom row of Figure 12, though there exists a noticeable scatter.

Nonetheless, the found correlation prompts the question of what impact a high centershift has on *individual* substructure masses for a given projection. To this end, the projections of the galaxy clusters within the "giants" mass bin are split into four groups based on their centershift. Then, the resulting fractional projected substructure masses $f_{\rm x} = M_{\rm cyl}/M_{\rm tot}$ are depicted in Figure 13 as a function of the most massive bound subhalo mass fraction $M_{\rm sub}/M_{\rm tot}$ within their aperture. The colors denote the different ranks of the substructures, from f_1 the first substructure shown in purple to the eighth-most massive substructure f_8 shown in pink.

We find the mass fractions f_1 of the first substructures to generally increase with decreasing centershift, while the mass fractions of the second to eighth substructure decrease. For high centershifts s, there are multiple cases where the most massive substructure (purple) lies at a low value of $M_{\rm s}$ (on the order of $1\% \cdot M_{\rm tot}$). This is exceedingly rare for low centershifts s, where instead the most massive substructure also typically lies at the deepest point of the potential (hence it contains the SUBFIND center of the cluster).

The horizontal black lines in Figure 13 denotes the mass fraction f_8 of the eighth substructure of A2744. For the lowest centershift bin, there are only 23 of 1450 projections with a fifth substructure (olive) where the substructure mass fraction f_5 lies above this black line. Not a single sixth substructure reaches a mass fraction comparable to the eighth substructure mass fraction of A2744. For the highest centershift bin, this occurs more frequently even for the eighth substructure (pink), with 57

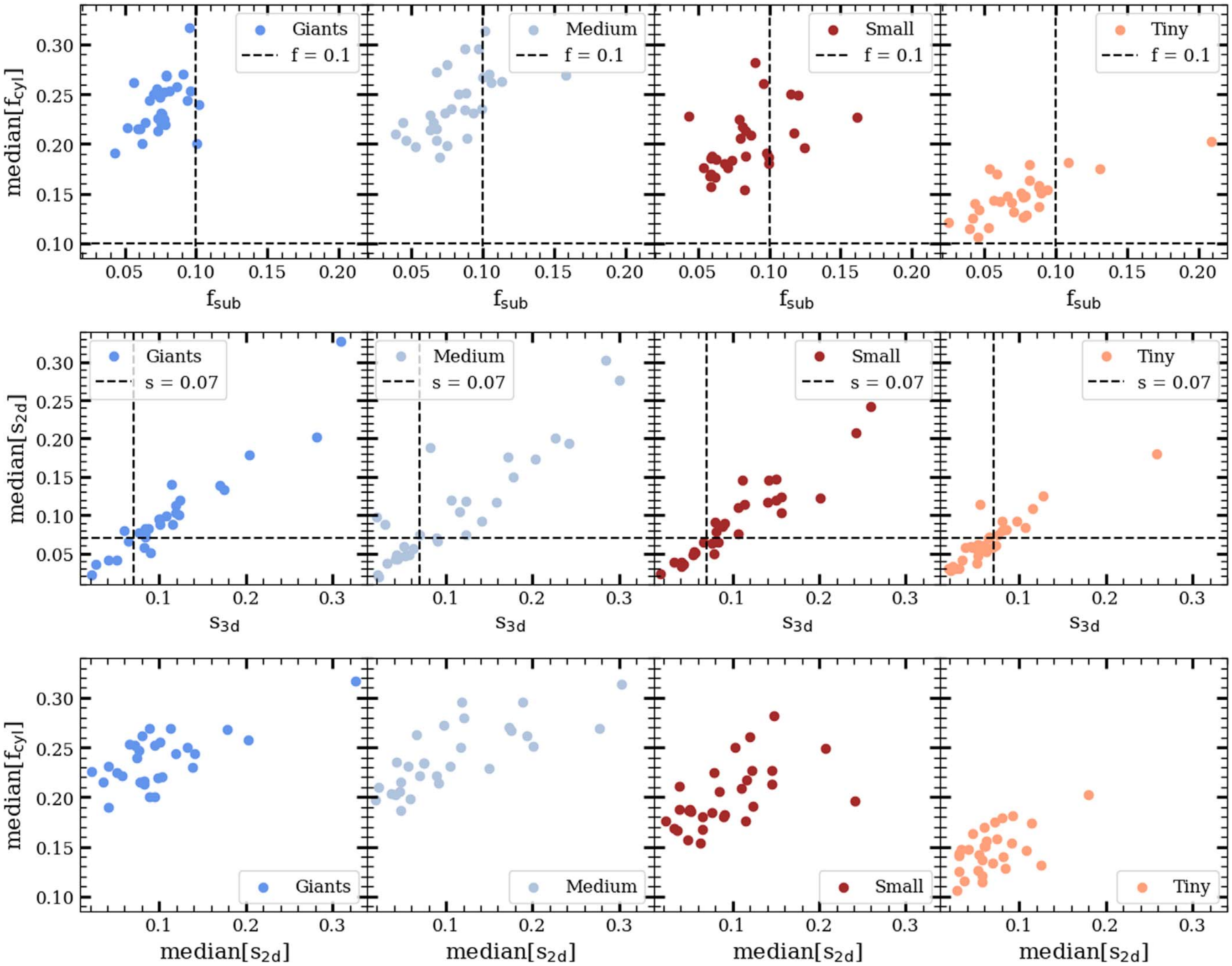

Figure 12. Median projected values of *f* (top row) and *s* (middle row) over the 200 random projections for each galaxy cluster as a function of their three-dimensional values, as well as the relation between projected *f* and *s* (bottom row). The dashed lines denote typical thresholds, with higher values indicative of a dynamically active galaxy cluster.

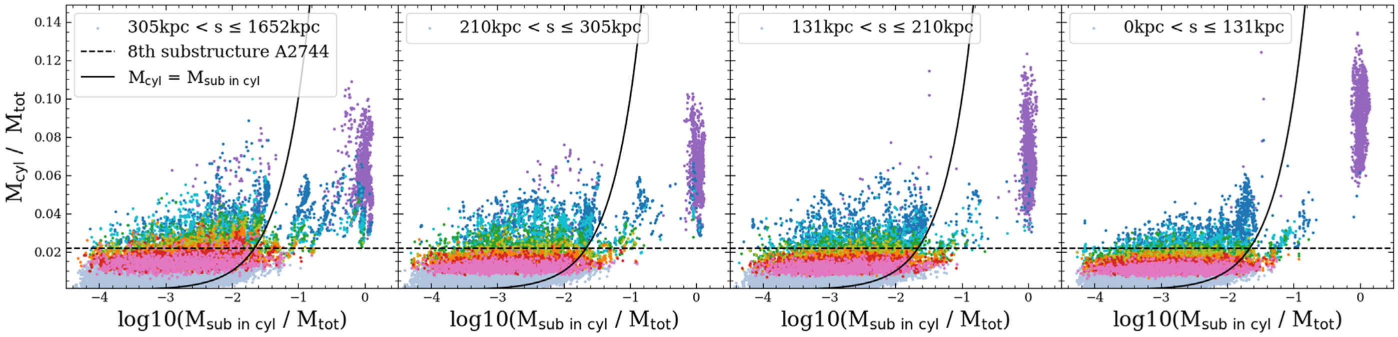

Figure 13. The substructure mass divided by the total mass within 1.3 Mpc is projected as a function of the most massive bound subhalo mass M_s within their aperture. The projections are split into quartiles by their centershift (each containing 1450), going from *left* to *right* as highest to lowest, with borders as given in the legends. Within each projection, the first to eighth-most massive substructures are colored as purple, blue, cyan, green, olive, orange, red, and pink, with all others colored gray. The horizontal black line denotes the mass fraction of the eighth substructure of A2744, such that all pink points that lie above it belong to a projection with a comparable substructure mass distribution. This is the case for 57, 1, 0, and 0 projections when going from left to right. The black dashed curve denotes equality between projected and bound mass.

of 1450 projections having an eighth substructure with a mass fraction f_8 larger or comparable to A2744. There is only one projection with an eighth substructure mass fraction f_8 above the line that does not lie in the bin of highest centershift, and it instead lies in the bin with the second highest. We conclude that multiple massive substructures can only be found in nonrelaxed clusters with large centershifts, even if in return a large centershift does not necessarily indicate a large number of massive substructures. This is because a single major merger that is not yet relaxed can also lead to a large centershift, but it may result in only two massive substructures.

We thus find that a high centershift enhances the likelihood to find a larger number of massive substructures. This can be understood when considering the relation of the line of sight to the feeding filaments or to the axis of a recent major merger. For the galaxy clusters where there is a dominant such axis, if one were to look straight along it, the substructures would appear clumped together and thus result in a lower centershift. This would also reduce the number of very massive substructures, as more than one of them may be projected into single apertures. Conversely, orientations looking at the axis perpendicularly will see a string of individual substructures sitting within a strongly elongated halo. This allows for a higher number of apertures with extreme masses, while the center of these mass clumps is somewhere in between, shifted strongly compared to the potential minimum, which will be inside the most massive of these substructures. Indeed, Eckert et al. (2015) find indications that the merger axis for A2744 is perpendicular to the line of sight, comparable to what we find here for galaxy cluster 20 of the "giants," as discussed in Section 5.1.

6. Summary and Conclusion

In this study, we compared substructure mass distributions of simulated galaxy clusters to those observed with gravitational lensing. Some of the observed galaxy clusters, especially A2744, exhibit such massive substructures that these were discussed to possibly be in tension with results from cosmological ΛCDM simulations. So far, previous studies have tried to solve the tension using dark matter only simulations. Here, for the first time, we used a fully hydrodynamical cosmological simulation to search for A2744 counterparts and study the substructure mass functions of galaxy clusters in projection.

To be able to compare the most massive structures in the known universe, a large volume simulation with proper resolution is required. To this end, we used the *Box2b/hr* of the hydrodynamical cosmological simulation suite Magneticum Pathfinder, one of the largest baryonic simulations currently available covering a volume of $(909\ \mathrm{cMpc})^3$. In this simulation volume, at $z = 0.252$, there are 29 galaxy clusters with masses above $M_{\mathrm{FOF}} \geqslant 10^{15} M_{\odot}$. Galaxies are resolved down to stellar masses $M_* \geqslant 5 \times 10^9 M_{\odot}$ when requiring halos to contain at least 100 stellar particles. While having more than 500 of such resolved member galaxies in the most massive cluster, this large dynamical range allows us to study galaxy cluster substructure properties down to $M_{\mathrm{vir}} \geqslant 10^{14} M_{\odot}$ with large significance.

We developed a procedure for determining substructure masses within galaxy clusters in projection, including subtracting a spherical model for the cluster, which more closely follows the procedure typically applied to observations. The properties of the substructures found through this procedure were then compared to those of the bound subhalos. These were directly determined from the three-dimensional particle distribution by the structure finder SUBFIND, which is commonly used to find subhalos in simulations, as well as to the observations of especially the extreme case of galaxy cluster A2744.

Using this method, we find that:

1. The total projected substructure mass generally is a factor of two to three larger than the total bound intrinsic subhalo mass. For some galaxy clusters, the spread in projected substructure mass fractions, f_{cyl}, varies by a factor of four, depending on the projection.
2. The contributions to the substructure masses from the residuals of the main halo, even after subtracting a spherical model, are more significant than those from additional subhalos projected in a line. We quantified this into a two-parameter model that, for a given subhalo mass and projected distance for a given host galaxy cluster mass, can produce an expected range of projected substructure masses within a factor of two for around 80% of the cases.
3. We can successfully reproduce the substructure mass fractions observed within A2744 by Jauzac et al. (2016). Nonetheless, it constitutes a rare projection. Of the 5800 total projections of galaxy clusters with mass above $1 \times 10^{15} M_{\odot}$, only 58 (108) have eight (seven) substructures with mass fractions comparable to the least massive substructure found in A2744.
4. Our best reproduction of the substructure mass fractions of A2744 occurs for a galaxy cluster that just recently underwent a massive major merger event with a merger ratio of 1:1.4, in addition to several minor merger events with mass ratios of 1:4, 1:6, and 1:24. We find that the appearance of multiple large substructures is a direct consequence of such recent multiple merger accretion events.
5. Furthermore, our simulated counterpart of A2744 exhibits strong noticeable shock fronts resulting from the post-core-passage major merger, in line with observations of strong shock fronts detected in A2744 (e.g., Owers et al. 2011; Rajpurohit et al. 2021). In addition, we find that the simulated counterpart of A2744 is fed through four main filaments, again in agreement with observations (Eckert et al. 2015).
6. In general, a large total substructure mass fraction correlates to a larger amount of recently accreted mass and the dynamical state of the cluster, in agreement with previous works by Neto et al. (2007) and Jiang & van den Bosch (2017). For the galaxy clusters with $M_{\mathrm{vir}} \geqslant 2 \times 10^{14} M_{\odot}$, this correlation persists even out to 3.2 Gyr, though it becomes quite scattered for the lower-mass clusters. This clearly indicates that the appearance of multiple massive substructures, independent of the host cluster mass, is a good tracer for (multiple) massive merger events occurring within the last 3.2 Gyr, not yet long enough ago to completely disrupt the substructures due to stripping and dynamical friction processes in the cluster environment. This timescale is longer than what was previously found from dark matter only simulations, showing that the deeper potential wells generated due to the presence of the baryons foster the longer survival times of the satellite galaxies (see also Bahé et al. 2019, for satellite galaxy survival timescales). Ultimately, this increases the time window of the appearance of large substructures—and therefore allows for more extreme configurations of total substructure mass fractions in hydrodynamical simulations compared to dark matter only ones.

7. Galaxy clusters whose eighth substructures have the highest (lowest) mass fractions out of our sample have gained a high (low) percentage of their mass within the last 2 Gyr, allowing for insight into the dynamical state and recent accretion history of the galaxy cluster without the requirement of having measured all substructure masses.
8. The mass of the observed galaxy cluster is not necessarily a guarantee that a significant fraction of the current cluster has been assembling already at high redshift, in agreement with results from protocluster evolution pathways by Remus et al. (2022). Instead, we find some of the most massive galaxy clusters to have reached masses above $1 \times 10^{14} M_{\odot}$ only recently, below $z = 1$, clearly demonstrating that some of the most massive nodes in the cosmic web have been assembled in very complex ways, being the result of larger numbers of smaller systems merging together on comparatively shorter timescales. Multiple massive substructures might be a good indicator for such nodes; however, the present sample of massive galaxy clusters is too small to provide statistically representative conclusions on that matter.
9. The necessary condition for finding a large number of massive substructure masses is a high centershift. This means that the galaxy cluster must be dynamically active *as well as* observed from a projection angle where the substructures are distributed largely perpendicular to the line of sight. Such in-plane geometry then also fosters the detectable appearance of other indications of dynamically strongly disturbed systems, such as the presence of radio relics.

We conclude that, given the importance of galaxy cluster substructures for quantifying the clusters dynamical state as well as for constraining models of dark matter (Bhattacharyya et al. 2021), it is of great importance to consider in detail the impact of projection effects when comparing measurements to cosmological simulations. The findings here further demonstrate that the total substructure mass fraction $f_{\rm cyl}$, even when measured in projection, indicates dynamically active galaxy clusters and still correlates well with the mass accretion history of the cluster.

Finally, we have shown that we can successfully reproduce not just the substructure mass fractions but also other properties of the extreme galaxy cluster A2744 in the hydrodynamical cosmological Magneticum Pathfinder simulation within the ΛCDM framework, demonstrating that there is no tension between ΛCDM and the existence of such massive substructures. Instead, we showed that such special galaxy clusters are rather interesting in terms of their accretion histories, and that they could be tracing special nodes of particularly late assembly in the cosmic web—which, however, remains to be further analyzed in future studies.

L.C.K. and K.D. acknowledge support by the COMPLEX project from the European Research Council (ERC) under the European Unions Horizon 2020 research and innovation program grant agreement ERC-2019-AdG 882679. The *Magneticum* simulations were performed at the Leibniz–Rechenzentrum with CPU time assigned to the Project *pr83li*. This work was supported by the Deutsche Forschungsgemeinschaft (DFG; German Research Foundation) under Germany's Excellence Strategy—EXC-2094-390783311. We are especially grateful for the support by M. Petkova through the Computational Center for Particle and Astrophysics (C2PAP). Plotting is done via matplotlib by Hunter (2007), and Gaussian fitting performed using the JULIA "Distributions.jl" package by Besançon et al. (2021).

Appendix A
The Gaussian Distribution of Substructure Masses

To see the distribution of substructure masses within a given subhalo mass bin $M_{\rm s}$, Figure 14 considers all substructures whose most massive bound subhalo has a mass of $6 \times 10^{11} M_{\odot} \leqslant M_{\rm s} < 8 \times 10^{11} M_{\odot}$. This mass bin is split then further into ten radial bins by their projected distance. The resulting distribution of $M_{\rm cyl}$ (blue histogram) in each bin is largely Gaussian in nature, which can be seen from the direct fits (orange dashed curves). Using the mean mass $\bar{M}_{\rm s} = 7.1 \times 10^{11} M_{\odot}$ and the mean radius $\bar{r}_{\rm 2d}$ of each radial bin allows a predicted distribution of $M_{\rm cyl}$ to be made via Equations (8) and (12), which is shown as black curves. As can be seen, the prediction well captures the real distribution of substructure masses.

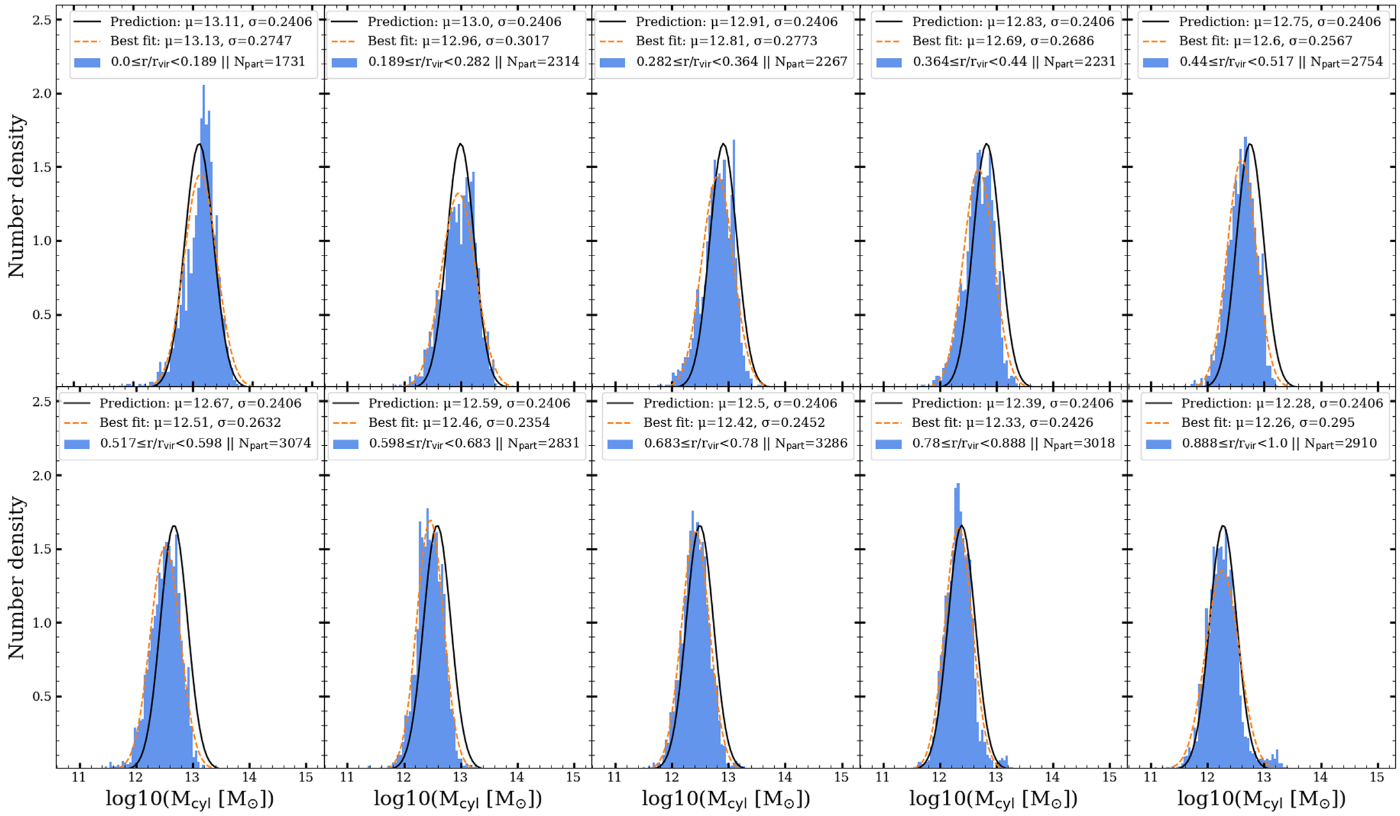

Figure 14. The distribution of substructure masses M_{cyl} for an example bin in subhalo mass, $6 \times 10^{11} M_{\odot} \leqslant M_{\mathrm{s}} < 8 \times 10^{11} M_{\odot}$. Plotted are different ranges of $r_{2\mathrm{D}}$ as written in the legend, going from lowest to highest projected distance as left to right, then top to bottom. The blue histograms depict the distribution of determined M_{cyl}. Black solid lines are the predicted distributions of projected mass from Table 3 via Equation (12), while the orange dashed lines are the best-fit single Gaussian models to the M_{cyl}, with mean and variance as given in the legend for both.

Appendix B
The Impact of Varying Projection Depth

To determine the impact of varying projection depths on the results presented, Figure 15 considers, for two different projection depths, two galaxy clusters—number 5 (left) and number 20 (right)—of the "giants" mass bin. They are chosen because they represent a highly relaxed and a disturbed cluster, respectively (see, e.g., Figure 1). Their fractional substructure mass for their eight most massive ones is depicted through a violin plot, with the blue error bars denoting the overall spread in the 200 projections while the frequency of mass fractions for each substructure number is represented through the blue shaded area. The black line denotes the mean mass over all orientations. First, the top row with the typical projection depth $r_z \approx 5 \cdot r_{\mathrm{vir}}$ is considered.

Galaxy cluster 5 exhibits a noticeably more peaked distribution, with orientations being quite similar in their substructure mass fractions, especially for the higher numbers, while in contrast number 20 has a generally flatter slope and a larger variance in the mass fractions of higher-number substructures. This can also be seen with regard to the black dotted line representing a value slightly above 2% of the total mass, which for galaxy cluster 5 is only achieved very rarely for substructure number 5 and is common only for substructure 2, while galaxy cluster 20 has this occur even more frequently for substructure numbers as high as 8 and regularly makes this threshold for substructures up to number 5. It is interesting to note the bimodal behavior in the frequencies of mass fractions that appears for galaxy cluster 20 and is especially noticeably in the first and third substructure. Here, two distinct peaks are visible, indicating that there are two classes of orientations for this galaxy cluster: a more common one with a lower first substructure mass and another, more rare one with a first mass nearly 1.5 times as high. Even for the seventh and eighth substructures, there is still a significant spread possible between the masses, unlike for galaxy cluster 5.

The bottom row of Figure 15 depicts the same for a projection depth of $r_z = 1 \cdot r_{\mathrm{vir}}$ (before and behind the cluster) to test how relevant fore-/background structures are. Little difference overall is found to the usual projection depth depicted in the top row. The first substructure mass for both clusters rises marginally, with the most noticeable difference being the absence of orientations with a small value for galaxy cluster 5. This implies that there exists in some projections a fore- or background structure that shifts the center of mass, thus reducing the first aperture's mass in some cases, while the cluster itself is entirely dominated by its brightest cluster galaxy. However, this does not strongly impact the distribution of the higher-number substructure masses, except for marginally reducing their maxima. This can be seen also for galaxy cluster 20, where the respective numbers of projections with an eighth substructure of mass fraction lying above the black line are three and one for the top and the bottom row. It follows that a deeper projection depth (i.e., less resolved redshift space) does marginally allow for larger peak masses of substructures in the cases where some additional objects are projected into the image, but the overall effect of projection of the galaxy cluster is significantly larger than the impact from these additional structures.

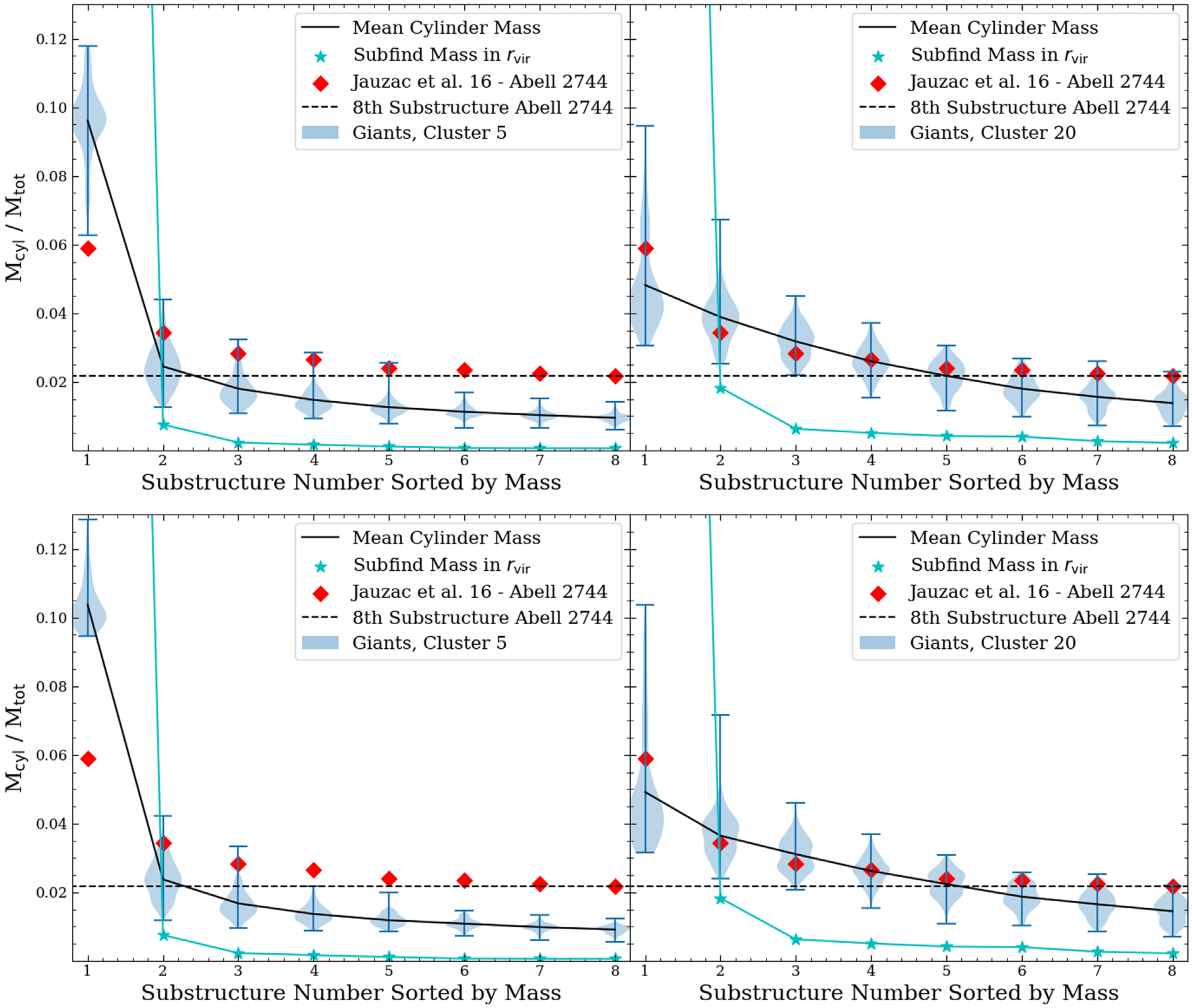

Figure 15. The distribution of the mass fractions for the eight most massive substructures within 1.3 Mpc for galaxy clusters 5 (left) and 20 (right) of the "giants" mass bin for all 200 orientations out to the typical projection depth r_z (top row) and out to $r_{\rm vir}$ (*bottom row*). Blue error bars denote the overall spread, while the blue shaded area represents the percent number of orientations at each mass fraction, with a larger bulge meaning a larger percentage. Dashed black line equals a mass fraction of around 2.2%.

ORCID iDs

Veronica Biffi https://orcid.org/0000-0001-9260-3826

References

Allen, S. W., Rapetti, D. A., Schmidt, R. W., et al. 2008, MNRAS, 383, 879
Bahé, Y. M. 2021, MNRAS, 505, 1458
Bahé, Y. M., Schaye, J., Barnes, D. J., et al. 2019, MNRAS, 485, 2287
Beck, A. M., Murante, G., Arth, A., et al. 2016, MNRAS, 455, 2110
Bergamini, P., Acebron, A., Grillo, C., et al. 2023, A&A, 670, 60
Besançon, M., Papamarkou, T., Anthoff, D., et al. 2021, Journal of Statistical Software, 98, 1
Bhattacharyya, S., Adhikari, S., Banerjee, A., et al. 2022, ApJ, 932, 30
Biffi, V., Borgani, S., Murante, G., et al. 2016, ApJ, 827, 112
Biffi, V., Dolag, K., & Merloni, A. 2018, MNRAS, 481, 2213
Bird, J. P., & Goldberg, D. M. 2018, MNRAS, 476, 1198
Boschin, W., Girardi, M., Spolaor, M., & Barrena, R. 2006, A&A, 449, 461
De Lucia, G., Kauffmann, G., Springel, V., et al. 2004, MNRAS, 348, 333
Dolag, K., Borgani, S., Murante, G., & Springel, V. 2009, MNRAS, 399, 497
Dolag, K., Jubelgas, M., Springel, V., Borgani, S., & Rasia, E. 2004, ApJL, 606, L97
Dolag, K., Mevius, E., & Remus, R.-S. 2017, Galax, 5, 35
Dolag, K., Vazza, F., Brunetti, G., & Tormen, G. 2005, MNRAS, 364, 753
Donnert, J., Dolag, K., Brunetti, G., & Cassano, R. 2013, MNRAS, 429, 3564
Eckert, D., Jauzac, M., Shan, H., et al. 2015, Natur, 528, 105
Eckert, D., Jauzac, M., Vazza, F., et al. 2016, MNRAS, 461, 1302
Einasto, J. 1965, TrAlm, 5, 87
Fabjan, D., Borgani, S., Tornatore, L., et al. 2010, MNRAS, 401, 1670
Giovannini, G., Tordi, M., & Feretti, L. 1999, NewA, 4, 141
Grillo, C., Suyu, S. H., Rosati, P., et al. 2015, ApJ, 800, 38
Harris, W. E., Remus, R.-S., Harris, G. L. H., & Babyk, I. V. 2020, ApJ, 905, 28
Hirschmann, M., Dolag, K., Saro, A., et al. 2014, MNRAS, 442, 2304
Hunter, J. D. 2007, CSE, 9, 90
Jauzac, M., Eckert, D., Schwinn, J., et al. 2016, MNRAS, 463, 3876
Jiang, F., & van den Bosch, F. C. 2016, MNRAS, 458, 2848
Jiang, F., & van den Bosch, F. C. 2017, MNRAS, 472, 657
Kassiola, A., & Kovner, I. 1993, ApJ, 417, 450
Kempner, J. C., & David, L. P. 2004, MNRAS, 349, 385
Komatsu, E., Smith, K. M., Dunkley, J., et al. 2011, ApJS, 192, 18
Lotz, J. M., Koekemoer, A., Coe, D., et al. 2017, ApJ, 837, 97
Lotz, M., Dolag, K., Remus, R.-S., & Burkert, A. 2021, MNRAS, 506, 4516
Lotz, M., Remus, R.-S., Dolag, K., Biviano, A., & Burkert, A. 2019, MNRAS, 488, 5370
Mahler, G., Richard, J., Clément, B., et al. 2018, MNRAS, 473, 663

Mao, T.-X., Wang, J., Frenk, C. S., et al. 2018, MNRAS, 478, L34
Martin, G., Bazkiaei, A. E., Iodice, M. S. E., et al. 2022, MNRAS, 513, 1459
Meneghetti, M., Davoli, G., Bergamini, P., et al. 2020, Sci, 369, 1347
Merten, J., Coe, D., Dupke, R., et al. 2011, MNRAS, 417, 333
Munari, E., Grillo, C., De Lucia, G., et al. 2016, ApJL, 827, L5
Navarro, J. F., Frenk, C. S., & White, S. D. M. 1996, ApJ, 462, 563
Neto, A. F., Gao, L., Bett, P., et al. 2007, MNRAS, 381, 1450
Okabe, N., Futamase, T., Kajisawa, M., & Kuroshima, R. 2014, ApJ, 784, 90
Owers, M. S., Randall, S. W., Nulsen, P. E. J., et al. 2011, ApJ, 728, 27
Power, C., Navarro, J. F., Jenkins, A., et al. 2003, MNRAS, 338, 14
Ragagnin, A., Dolag, K., Biffi, V., et al. 2017, A&C, 20, 52
Ragagnin, A., Dolag, K., Moscardini, L., Biviano, A., & D'Onofrio, M. 2019, MNRAS, 486, 4001
Ragagnin, A., Fumagalli, A., Castro, T., et al. 2021, arXiv:2110.05498
Ragagnin, A., Meneghetti, M., Bassini, L., et al. 2022, A&A, 665, 16
Rajpurohit, K., Vazza, F., van Weeren, R. J., et al. 2021, A&A, 654, A41
Remus, R.-S., Dolag, K., & Dannerbauer, H. 2022, arXiv:2208.01053
Remus, R.-S., Dolag, K., & Hoffmann, T. 2017, Galax, 5, 49
Remus, R.-S., & Forbes, D. A. 2022, ApJ, 935, 37
Retana-Montenegro, E., van Hese, E., Gentile, G., Baes, M., & Frutos-Alfaro, F. 2012, A&A, 540, A70
Schulze, F., Remus, R.-S., Dolag, K., et al. 2018, MNRAS, 480, 4636
Schwinn, J., Baugh, C. M., Jauzac, M., Bartelmann, M., & Eckert, D. 2018, MNRAS, 481, 4300
Schwinn, J., Jauzac, M., Baugh, C. M., et al. 2017, MNRAS, 467, 2913
Springel, V. 2005, MNRAS, 364, 1105
Takada, M., & Jain, B. 2003, MNRAS, 340, 580
Teklu, A. F., Remus, R.-S., Dolag, K., et al. 2015, ApJ, 812, 29
Tornatore, L., Borgani, S., Dolag, K., & Matteucci, F. 2007, MNRAS, 382, 1050
Tornatore, L., Borgani, S., Matteucci, F., Recchi, S., & Tozzi, P. 2004, MNRAS, 349, L19
Treu, T., Roberts-Borsani, G., Bradac, M., et al. 2022, ApJ, 935, 110
Wiersma, R. P. C., Schaye, J., & Smith, B. D. 2009, MNRAS, 393, 99